



A Hydro-Mechanical Investigation of the First M 4 + Seismicity Sequence in the Midland Basin, Texas

Lei Jin¹ · William J. Curry¹ · Stefan A. Hussenoeder²

Received: 13 May 2024 / Accepted: 2 August 2024
© The Author(s) 2024

Abstract

The M 4.2 2020 December Stanton, TX seismicity sequence marks the first of several M 4 + seismicity sequences in the Midland Basin. In this study, we investigate its causal link to the surrounding field-scale, multi-decadal, multi-zone saltwater disposal (SWD) by 180 + SWD wells through integrated data analysis and high-end hydro-geomechanical numerical modeling. We test six scenarios by permutating three fault upper extents and two fault-zone structures and interpret their plausibility based on their performance in reproducing seismicity onset and distribution as characterized by an aggregated earthquake catalog. We do so via Coulomb faulting analysis at inferred seismogenic depths complemented by rate-and-state friction-based seismological modeling on the event-hosting fault. Our analysis suggests that the basement-rooted faults, despite being poorly seen in the reflection seismic data, likely extend into the deep disposal interval but not the two shallower disposal intervals and contain impermeable fault gouge. The work also strongly suggests that the seismicity sequence was induced mainly by intermediate and deep SWD and negligibly by shallow SWD through an over three-decadal stressing process involving 10 + wells up to 60 km laterally away from the event epicenters. The joint stressing by a cluster of wells to the Northwest and a near-fault well produced two Coulomb stress lobes that explain the bifurcating seismicity near the top of the basement. Meanwhile, the mainshock was likely preceded by a half-year-long nucleation period, over which the joint stressing also drove the development of a seismicity funnel zone that explains the remaining seismicity in the basement.

Highlights

- We investigate the origin of the 1st M 4 + seismicity sequence in the Midland Basin via data integration and high-end finite element modeling
- We test six scenarios and infer their plausibility using Coulomb faulting and earthquake nucleation analysis
- The analysis helps constrain fault dimension and permeability structure
- Seismicity was driven mainly by intermediate and deep SWD involving 10 + wells dating back 30 + years
- There likely was a nucleation effect in the triggering process

Keywords Saltwater disposal · Poroelasticity · Hydro-mechanical coupling · Induced seismicity · Earthquake nucleation · Finite element modeling

1 Introduction

Fluid injection such as saltwater disposal (SWD) into the subsurface can induce earthquakes (Wesso and Nicholson 1987; Ellsworth 2013; National Research Council 2013). There has been an increase in seismicity associated with SWD activities in several states in the United States in the last decade (e.g., Frohlich et al. 2011; Kim 2013; Keranen et al. 2014; Rubinstein et al. 2014; Walsh and Zoback 2015),

✉ Lei Jin
lei.jin@exxonmobil.com

¹ ExxonMobil Technology and Engineering Company, Spring, TX, USA

² ExxonMobil Upstream Company, Spring, TX, USA

and most recently in the Permian Basin (e.g., Savvaidis et al. 2019; Skoumal and Trugman 2021; Skoumal et al. 2021; Woo and Ellsworth 2023). Traditionally, induced earthquakes are distinguished from natural ones according to a set of empirical criteria based on their spatial–temporal correlation with injection activities and deviation from regional background seismicity trends (e.g., Davis and Frohlich 1993). The correlative approach has since evolved, adding analysis such as earthquake relocation and focal mechanism inversion (Kim 2013), seismicity delineation relative to local faults (Frohlich et al. 2016), V_p -to- V_s ratio time series characterization (Improta et al. 2015), and seismicity space–time clustering (Savvaidis et al. 2020), to support the association of seismicity with fluid injection.

While data correlation provides useful insights, causal investigation of seismicity fundamentally requires mechanistic analysis. Classically, the triggering of seismicity is conceptualized as a hydro-shearing process (Byerlee 1978), the onset of which is described by the Coulomb faulting theory that builds upon the simple effective stress principle suitable for a fault (Jaeger and Cook 1979). The frictional failure criterion outlines pore pressure and stress perturbations as two potential fault-destabilizing sources. Correspondingly, two main triggering mechanisms have been widely considered so far—pore pressure diffusion (Hsieh and Bredehoeft 1981) and coupled pore pressure diffusion and poroelastic stressing (Rozhko 2010; Segall and Lu 2015). Other mechanisms related to seismic or aseismic slip-induced stress transfers also exist, as summarized by Ge and Saar (2022). Using the first mechanism requires first obtaining pore pressure changes from hydrological modeling and this has been done in some correlative studies to further support causal assessment (e.g., Keranen et al. 2013; Peterie et al. 2018; Chen et al. 2018; Grigoratos et al. 2020). Adopting the second mechanism relies on coupled hydrological and geomechanical modeling to obtain interacting pore pressure and stress perturbations. This is done by solving coupled mass and force balance laws constituting a poromechanical governing framework. Perhaps the most well-known framework is the Biot poroelasticity, first introduced for a fluid-saturated, linearly diffusive, and linearly elastic porous rock (Biot 1941) and subsequently recast using physically more interpretable parameters (Rice and Cleary 1976). Other frameworks are available, offering an extension to unsaturated, adsorptive, non-isothermal, large-deformational, and fractured regimes (e.g., Coussy 2004; Borja 2006; Dassault Systèmes Simulia 2014; Jin and Zoback 2017).

The coupled hydro-mechanical triggering mechanism is favored between the two main mechanisms as it naturally subsumes the pore pressure diffusion triggering mechanism in theory and uncovers additional details (Jin 2022). The coupled mechanism has also been used to explain several

notable recent induced seismicity sequences in Alberta, Oklahoma, and Texas (e.g., Deng et al. 2016; Fan et al. 2016; Goebel et al. 2017; Chang and Yoon 2020, 2022; Tung et al. 2021; Haddad and Eichhubl 2023). Utilization of the mechanism to explain seismicity relies on solutions, either analytical or numerical, to poroelastic governing equations. Therefore, from a modeling perspective, we must first ensure the quality of the solutions, and this is achieved by addressing two main challenges. The first challenge is to implement poroelasticity properly. Sometimes, this is done using commercial software such as Abaqus (Dassault Systèmes Simulia 2014). Because Abaqus was originally designed to model unsaturated soil consolidation, Altmann et al. (2010) proposed an equivalent parameter mapping approach to mimic Biot poroelasticity in Abaqus. This practice was retained in some later studies (e.g., Fan et al. 2016; Haddad and Eichhubl 2020). Jin (2023) proved that the governing conservational and constitutive framework formulated in Abaqus is general, naturally capturing two orders of fluid–solid coupling without prior postulations on 1st-order monolithic coupling underlying Biot poroelasticity. The general framework also reduces to Biot poroelasticity under simplifying conditions. Hence, we advocate for directly implementing the general poroelasticity in Abaqus following proper procedures. This approach captures additional coupling compared to implementing Biot poroelasticity in other software such as COMSOL (2014) as was done in Chang and Yoon (2020, 2022), or using the increasingly popular open-source code POEL based on Wang and Kumpel (2003); Zhai et al. (2021); Tung et al. (2021) and Tan and Lui (2023). The second challenge is to build a model with sufficient details. Previous case studies have relatively simple model configurations consisting of a single deep disposal interval overlaying the crystalline basement and a few deep wells with simple injection histories; also, they either do not include faults or include several basement-rooted faults that are simply distributed. Sometimes, a simplified model may not adequately capture possible controlling factors to arrive at plausible triggering scenarios. For example, it has been shown that seismicity in some cases is driven mainly by shallow SWD rather than deep SWD (Zhai et al. 2021; Tan and Lui 2023); even within a single deep disposal interval, including more distal wells is necessary to explain seismicity (Haddad and Eichhubl 2023); fault-zone structures strongly control the size of earthquake nucleation patch and the duration of nucleation phase (Snell et al. 2020), and help better explain deep seismicity sometimes (Ortiz et al. 2019); variable-rate injection can lead to drastically different hindcast of seismicity rate, by one order of magnitude, compared to constant-rate injection with equivalent volume, and better agrees with observation (Barbour et al. 2017). Therefore, we advocate for including, whenever possible, geologic, and

operational details such as multiple disposal intervals, formation topographies, faults, fault-zone structures, proximal and distal wells, and detailed variable injection histories spanning over decades.

Coupled hydro-mechanical modeling yields pore pressure and tensorial stress. The two are then used to calculate the Coulomb stress, also referred to as the Coulomb Failure Function (CFF) (e.g., Harris and Simpson 1992), which drives seismicity. Within the Coulomb faulting framework, once an area on the fault reaches its failure state, seismicity occurs instantaneously in the critical area. A large body of studies have demonstrated that Coulomb faulting analysis alone suffices to explain seismicity onset (e.g., Deng et al. 2016; Fan et al. 2016; Goebel et al. 2017; Grigoli et al. 2018; Schoenball et al. 2018; Chen et al. 2020; Hui et al. 2021; Wang et al. 2021; Smith et al. 2022). In other cases, however, the Coulomb faulting framework tends to underperform, such as yielding significantly earlier onset (e.g., Acosta et al. 2023) or requiring unusual parametrization (e.g., Haddad and Eichhubl 2023). Furthermore, Coulomb faulting analysis offers little insight into seismological features such as nucleation time, rupture speed and extent, and earthquake magnitude, count, and distribution. To further support causal assessment, one can model co-seismic dynamic rupture from pore pressure and poroelastic loading and see if fluid injection leads to the observed seismological features (e.g., Jin and Zoback 2018; Szafranski and Duan 2020; Wang et al. 2022). Unfortunately, this is very challenging in itself. An alternative, initially proposed by Dieterich (1994) for an elastic medium and later recast by Segall and Lu (2015) for a poroelastic medium, is to model seismicity nucleation and relative seismicity rate based on the rate-and-state frictional law. This approach to seismological modeling is increasingly popular in studying earthquake sequences as it reveals the spatiotemporal evolution of seismicity and can further support causal analysis when analyzed against quality catalogs (e.g., Norbeck and Rubinstein 2018; Chang and Yoon 2020; Tung et al. 2021; Heimisson et al. 2022). There are other seismological modeling frameworks, based on such as fault patch discretization and criticality analysis (Dempsey and Suckale 2017), seismogenic index (Shapiro et al. 2010; Langenbruch and Zoback 2016; Langenbruch et al. 2018), modified and time-dependent Coulomb stress (Dahm and Hainzl 2022), and hybrid deterministic fracture-poro-mechanical and stochastic stress drop modeling (Jin 2022), among others.

At 20:44:19 on December 31, 2020, a M 4.2 seismicity sequence occurred about 11 miles north of Stanton, Texas, according to the Texas Seismic Monitoring Network (TexNet 2021). The occurrence bears significance as it marks the first of several M 4+ seismicity sequences in the historically aseismic Midland Basin excluding the Horseshoe

Atoll region. The Railroad Commission of Texas Oil and Gas Division (2022) subsequently established the Stanton Seismic Response Area, citing that SWD was likely contributing to seismic activity in this area according to their analysis of available information. In this study, we conduct a detailed investigation into the triggering of the Stanton M 4.2 seismicity sequence in relation to the multi-decadal multi-zone SWD in the area through data integration and analysis and high-end numerical modeling. The modeling part builds upon our previous work establishing the methodology and workflow for three-dimensional (3D) fully coupled hydro-mechanical modeling of SWD in a layered, faulted, and poroelastic media (Jin 2023; Jin et al. 2023), and differs from existing studies in two ways. First, we use a general poromechanics framework and implement it in Abaqus in the limit of isothermal condition, full saturation, and no adsorption. The model captures a wider range of coupling beyond Biot's monolithic 1st-order coupling. Second, our model includes some previously unreported details, such as numerous wells sampling three disposal intervals, four decades of monthly injection rate, accurately preserved formation tops, and a network of basement-rooted faults with fault-zone architecture, requiring significantly higher modeling and computational efforts. Because of uncertainties in fault upper extent due to poor quality of 3D reflection seismic data, and unknown fault-zone structure, we test various fault scenarios. In each scenario, we cast the modeled pore pressure and poroelastic stress changes into the coupled triggering mechanism, and perform Coulomb faulting analysis and, if necessary, rate-and-state friction-based seismological modeling to account for potential nucleation effect. We interpret the plausibility of all scenarios based on their ability to hindcast seismicity onset and explain seismicity distribution. Along the way, we evaluate contributions by different disposal intervals, identify source stressors, replicate potential triggering processes, and elucidate the roles of faults, fault-zone structures, and the stress barrier, among others. Details are below.

2 Data and Analysis

2.1 SWD Wells, Faults, and Seismicity

We center our field-scale model around the M 4.2 event epicenter reported by TexNet (2021) and choose a 2500 km² (\approx 900 mile²) square as the area of study, see Fig. 1a. The area covers the central portion of the Midland Basin in Texas, occupying nearly the entire Martin County and extending to the East and South into adjacent counties. The area is historically aseismic but has experienced decades of SWD with recently elevated disposal rates

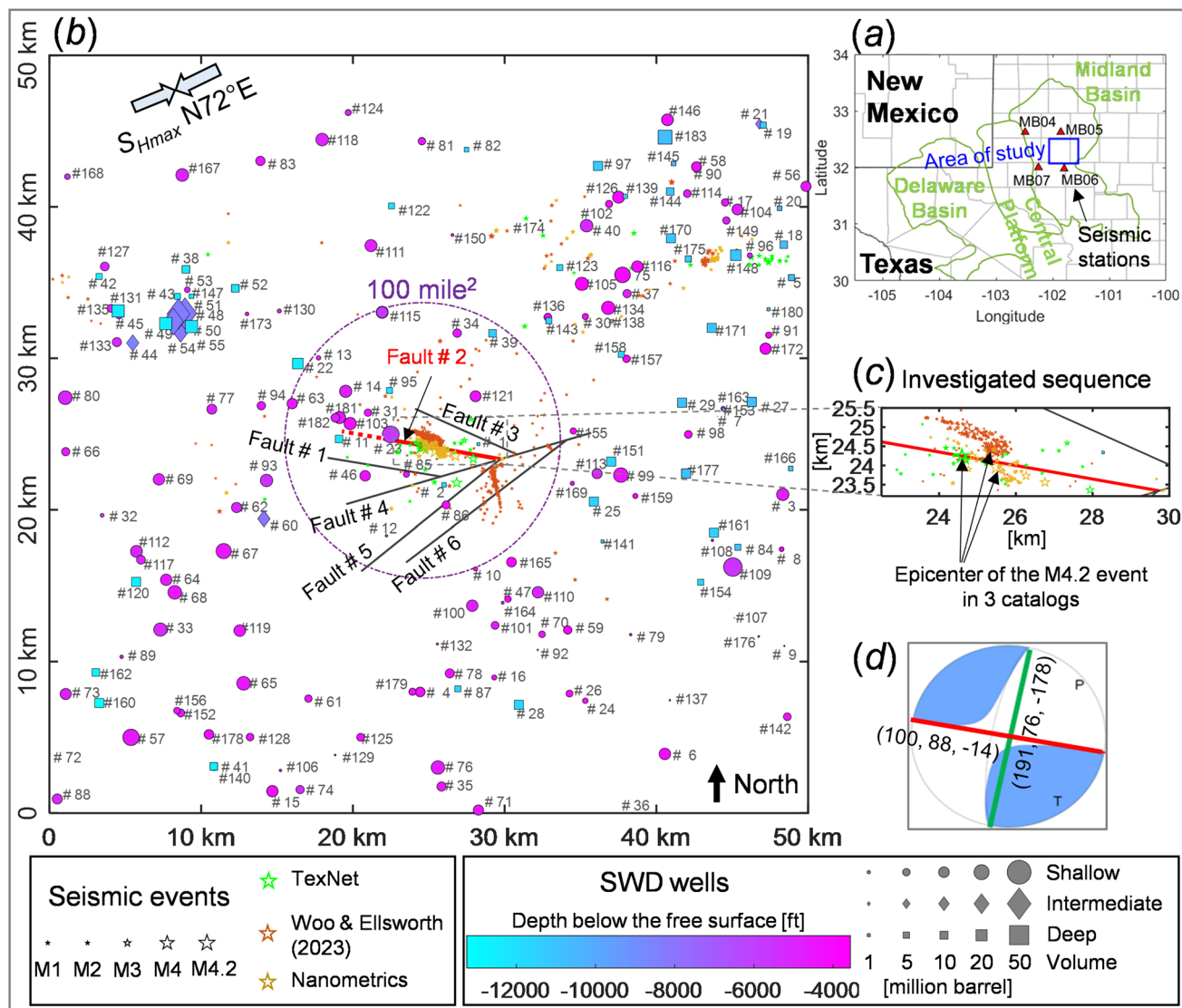


Fig. 1 Some basic information. **a** The area of study indicated by the blue box relative to the Permian Basin outlined in green. Four public regional seismic monitoring stations labeled MB04–MB07 are shown. **b** Map view of the SWD wells, faults, and earthquakes from three catalogs. The wells are numbered from 1 to 183 and the faults from 1 to 6. Shallow, intermediate, and deep wells are colored with their inferred disposal depths, sized with their cumulative disposal volume as of April 2021, and shaped as circles, diamonds, and squares, respectively. The faults are numbered from 1 to 6, and

together they form a herring-bone structured fault network. Fault #2 highlighted in red is the inferred seismogenic fault, with a less confidently interpreted segment indicated by a dashed line. The earthquakes are colored based on their source catalogs and sized with magnitudes. A 100-mile² circular area around the model center is shown for reference. **c** Close-up view of the earthquake sequence of interest. **d** Beach ball plot illustrating the focal mechanism of the M4.2 event with the main nodal plane shown in red (Color figure online)

(Sect. 2.2), suggesting a possible anthropogenic origin of the earthquakes. As of April 2021, when we performed the study, there were 183 active SWD wells within the area operated by 59 companies, with some distal wells up to 35 km away from the center. For each well, because its precise depth is unknown, we obtain the top and bottom of its permitted interval and use the midpoint to represent its disposal depth. Combined with knowledge of formation

tops (Fig. 2c), we show that the wells group into three disposal intervals—shallow, intermediate, and deep. The wells are then colored with their disposal depths, sized with their end cumulative disposal volumes (Fig. 3b), and shaped with their hosting disposal intervals, see Fig. 1b.

Faults in the area were largely unknown and unmapped until the occurrence of the earthquakes. Our interpretation of 3D reflection seismic data suggests the presence of a

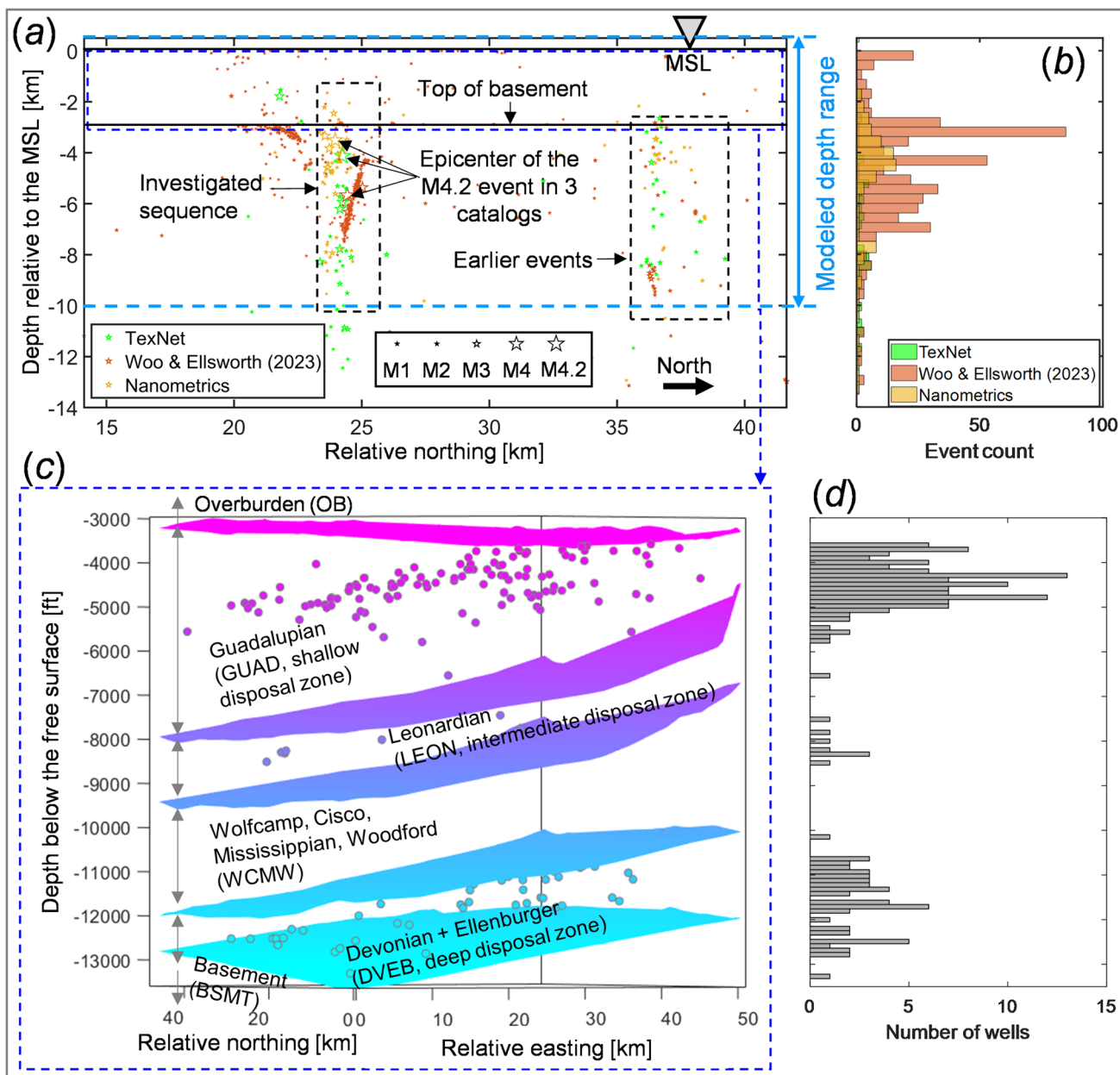


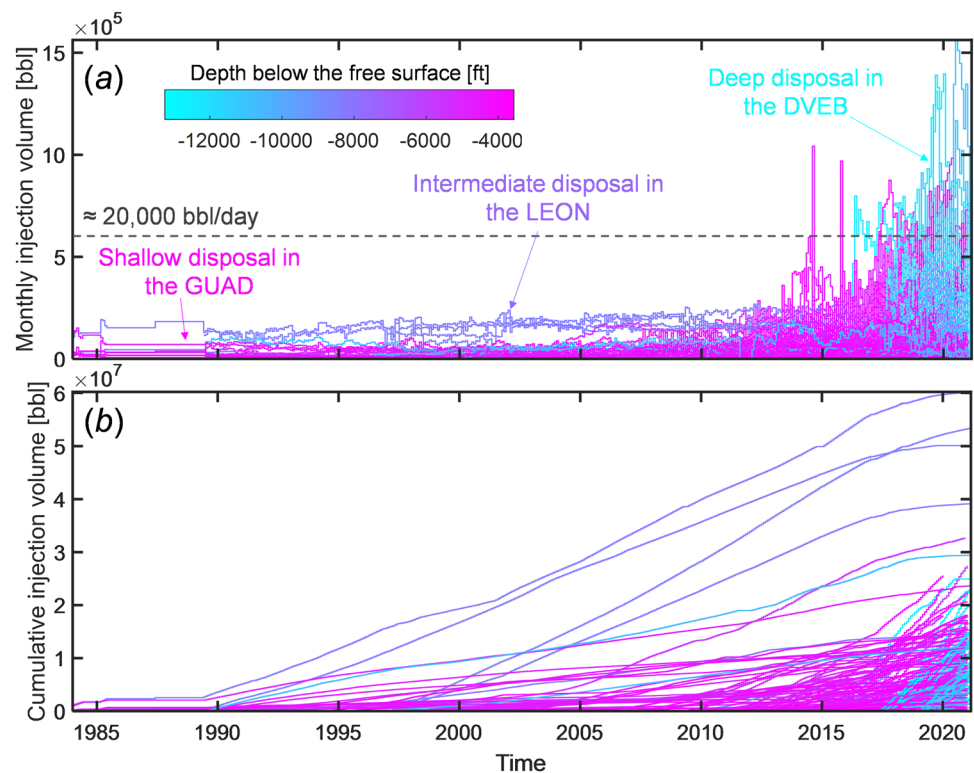
Fig. 2 Vertical distribution of the earthquakes, SWD wells, and formations. **a** West-facing cross-sectional view of the earthquakes from three catalogs relative to the mean sea level, the top of the basement, and the extent of our model. The investigated sequence and the earlier

far-field events are indicated. **b** Histogram of the event depths. **c** Distributions of the SWD wells relative to the formation tops. **d** Histogram of the SWD well depths

basement-rooted and herringbone-structured fault network consisting of one main fault and five secondary faults, see Fig. 1b. All faults have an interpreted dip of nearly 90° and are modeled as vertical in this study. The azimuths of faults labeled as #1–#6 are N99.4°E, N100.0°E, N114.2°E, N73.8°E, N51.1°E, and N52.7°E, respectively. For fault #2, we assign high confidence to the segment in solid red but low confidence to the segment to the west of well #23 in dash red. The two segments appear to be separated by a slightly Northeast trending feature, which is not modeled

here. For now, we model this uncertain segment as part of fault #2 with the same orientation but will allow for interpreting it as part of the rock in later analysis. Our fault interpretation, despite being done at an early stage, is overall consistent with a recent detailed fault mapping study (Horne et al. 2024), where the uncertain segment is left out. Furthermore, the upper extents of all these faults are hard to discern, due to their near-vertical nature. Addressing this uncertainty is elaborated in Sect. 3.4.

Fig. 3 Injection history is plotted as the monthly injection volume **a** and the cumulative injection volume **b** over time for all wells colored by their depths. Shallow, intermediate, and deep disposal are indicated, and the grey dashed line approximates 20,000 barrels per day per well disposal rate



For calibration and interpretation of our modeling outcomes, we obtain detailed earthquake data by aggregating three earthquake catalogs. These are the original TexNet (2021) catalog derived from the public regional seismic array, a recent high-quality catalog derived from private downhole arrays (Woo and Ellsworth 2023), and a Nanometrics subscriber catalog derived from a private local dense surface array. The three catalogs are plotted as stars in green, orange-red, and orange, respectively, sized with event magnitudes, see Fig. 1b. The events are also visualized in time in Appendix A.1, see Fig. 18. Notice all catalogs contain earlier far-field events, and the second catalog reveals an additional North–South trending branching fault, which is not modeled in this study. A close-up view of the investigated sequence is shown in Fig. 1c, where event epicenters cluster linearly along fault #2, suggesting its seismogenic state. This agrees with the focal plane solution of the M 4.2 event shown in Fig. 1d. The event is dominantly strike-slip with a minor normal component. The main nodal plane strikes at $N100^{\circ}E$ and dips at 88° , which is consistent with fault #2. Furthermore, a recent study by Lund Snee and Zoback (2018) shows that the area has a strike-slip faulting regime with the maximum horizontal principal stress S_{Hmax} striking at $N72^{\circ}E$, leading to a near-critical stress state on Fault #2, as detailed in Sect. 2.3. Considering these multiple lines of evidence, we infer that fault #2 hosted the main M 4.2 sequence.

Figure 2a illustrates the distribution of earthquakes over depth referenced to the mean sea level (MSL) and the top of the basement (TOB), and Fig. 2b is the associated histogram. In all three catalogs, the events are mostly located within the basement. However, the TexNet event hypocenters are more scattered and extend a few kilometers deeper, possibly due to uncertainties associated with limited station coverage and knowledge of the velocity model. Using detailed velocity models, recent seismology work (Sheng et al. 2022), and forward elastodynamic numerical modeling (Fang et al. 2024) both show that the events are shallower than reported by TexNet. This finding agrees better with the other two catalogs where the events rarely exceed 10 km in depth and tend to concentrate near the TOB. Considering these, our model extends from 0.5 km above the MSL to 10 km below, including nearly all hypocentral depths.

We also obtain the formation tops interpreted from 3D reflection seismic data in the area and the associated hydraulic and mechanical properties. Based on their contrasts, we divide the vertical section into 6 intervals, including 5 aggregated sedimentary layers and the crystalline basement (BSMT), see Fig. 2c. The SWD wells are located within the shallow Guadalupian (GUAD), the intermediate Leonardian (LEON), and the deep combined Devonian and Ellenburger (DVEB). Between the LEON and the DVEB are the Wolfcamp, Cisco, Mississippian, and Woodford formations, which are modeled as one combined interval (WCMW) in

this study. Figure 2d is a depth histogram of wells showing that most wells are shallow, some are deep, and several are intermediate.

2.2 Injection History

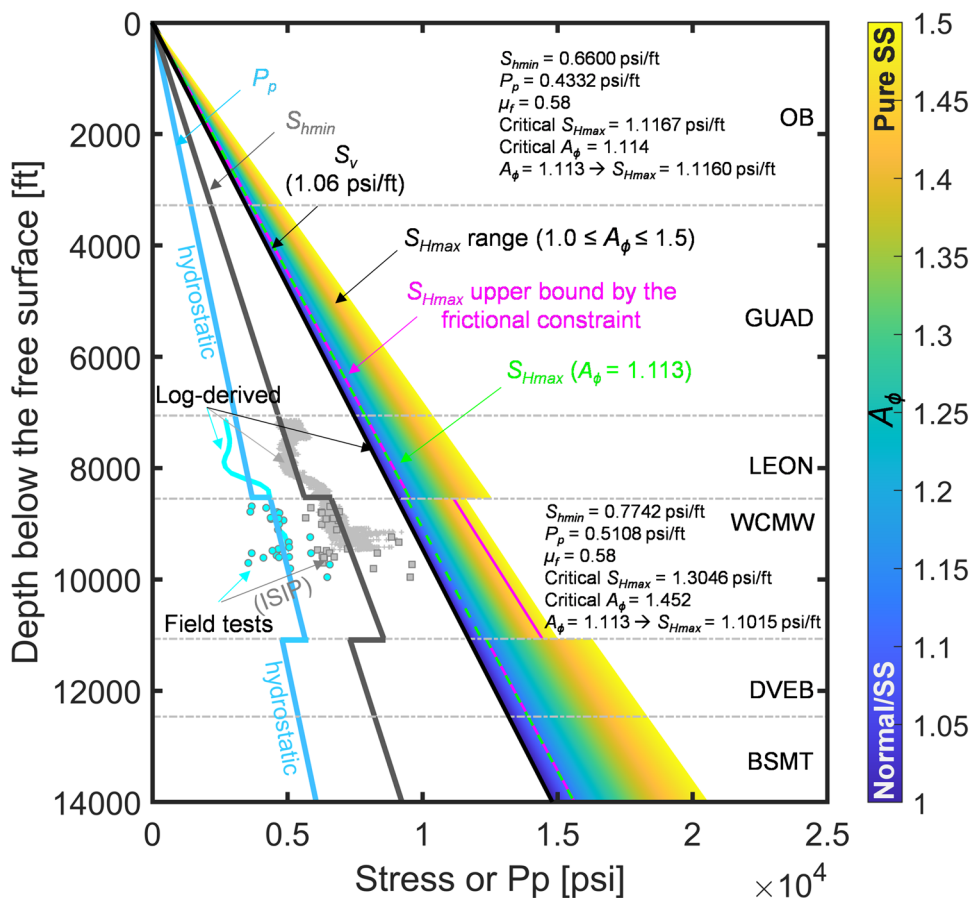
Figure 3 shows the monthly and cumulative injection volumes of all wells from the beginning of data reporting to April 2021. Shallow and intermediate wells began injecting in 1983 and have been ongoing ever since, whereas the deep injection mainly started after 2010. Both shallow and deep wells ramped up injection in 2015. The three disposal intervals from shallow to deep respectively received a total of about 911, 234, and 334 million barrels of saltwater from their in-zone wells. Inside each zone, wells #109, #54, and #183 discharged the most amount of saltwater, reaching around 33, 60, and 29 million barrels, respectively. Instead of focusing on the recent deep injection only (e.g., Tung et al. 2021; Chang and Yoon 2022), we include all historical injections because (1) a multi-decadal lag is possible between the beginning of injection (or depletion) and the onset of seismicity (e.g., Keranen et al. 2013; Smith et al. 2019), and (2) shallower injections are potentially important (Zhai et al. 2021; Tan and Lui 2023). The

monthly injection history of each well is strictly preserved in the modeling without data smoothing, as was done elsewhere (e.g., Haddad and Eichhubl 2023).

2.3 In-Situ Stress and Pore Pressure

Figure 4 shows the in-situ pore pressure and principal stresses used in this study. The faulting regime in the area is strike-slip with S_{Hmax} oriented at N72°E (Lund Snee and Zoback 2018), see also Fig. 1. We calculate the gradient of the overburden S_v from a density log, yielding 1.06 psi/ft. A recent Permian Basin-wide vertical stress model offers a nearly identical value in this area (Smye et al. 2021). Because S_v depends only on the density and does not vary, we use this value for all the intervals. We also obtain two datasets of the pore pressure P_p and the least horizontal principal stress S_{Hmin} . The first dataset, derived from well logs done from the LEON to the WCMW, suggests an increase in the gradients of both P_p and S_{Hmin} within the WCMW. The second dataset, sourced from field formation pressure tests and diagnostic fracture injection tests (DFIT) conducted within the WCMW, corroborates this trend. We use the instantaneous shut-in pressure (ISIP) to represent

Fig. 4 The in-situ pore pressure and stress model showing two sets of gradients within the MCMW and the remaining intervals. P_p is shown in cyan, S_{Hmin} in grey, S_v in black, and the possible range of S_{Hmax} for a strike-slip faulting regime in blue to yellow. The green dashed line indicates S_{Hmax} by assuming a constant A_ϕ of 1.11 (Lund Snee and Zoback 2018) over depth, whereas the magenta line indicates S_{Hmax} as an upper bound constrained by the frictional equilibrium theory (Zoback 2010). The latter is used for this study (Color figure online)



S_{hmin} (Zoback 2010) and find that the data points show good agreement with the log-derived S_{hmin} . Increased S_{hmin} gradient within shales has also been reported for other parts of the Midland Basin (e.g., Kohli and Zoback 2021) and other basins (e.g., Ma and Zoback 2020). The underlying mechanism lies in time-dependent creep and differential stress relaxation over geological time due to the viscoelastoplasticity of shales (Sone and Zoback 2014; Xu et al. 2017). Because S_v remains constant, S_{hmin} tends to converge toward S_v over time, resulting in decreased stress anisotropy. We, therefore, perform the least-squares fit of the data separately for the WCMW and the remaining intervals. This leads to a P_p gradient of 0.51 psi/ft within the MCMW and 0.43 psi/ft in others, the latter coinciding with a hydrostatic state.

The determination of S_{Hmax} is more challenging, especially in the absence of wellbore failure data that can be used to constrain S_{Hmax} (Zoback 2010). Using established P_p , S_{hmin} , and S_v , we first calculate the possible range of S_{Hmax} based on the given strike-slip faulting regime using an A_ϕ ranging from 1 to 1.5 (e.g., Hurd and Zoback 2012). Unfortunately, this yields a wide range of values. Meanwhile, we also use the frictional equilibrium constraint (Townend and Zoback 2000; Zoback 2010) to calculate the upper bound of S_{Hmax} . In all the intervals except the WCMW, this yields a critical S_{Hmax} gradient of around 1.12 psi/ft, corresponding to an A_ϕ of 1.11. This agrees with a recent stress map for the area (Lund Snee and Zoback 2018) assuming a coefficient of static friction μ_f of 0.58. This μ_f value is reasonable and consistent with the universally observed value of around 0.6 under high-stress environments typically experienced by deep sedimentary rocks and the crust (Byerlee 1978). Unlike in two recent studies which required an abnormally low μ_f of 0.35 to explain seismicity (Haddad and Eichhubl 2023), we retain this value in subsequent analysis. In the WCMW, the critical S_{Hmax} and the associated A_ϕ are 1.30 psi/ft and 1.45, respectively. On the other hand, assuming a constant A_ϕ of 1.11 by Lund Snee and Zoback (2018) over depth yields a S_{Hmax} gradient of 1.10 psi/ft within WCMW and 1.12 psi/ft within the other intervals. Considering that the relative stress magnitude can vary over depth, we opt for the former set of S_{Hmax} gradients, which are the upper bounds constrained by the frictional equilibrium theory, for this study.

2.4 Earthquake-Triggering Thresholds

Within the Coulomb faulting framework and given an orientation, depth, and in-situ pore pressure and principal stresses, a fault comes with an earthquake-triggering threshold, the breach of which requires an increase in its CFF. To arrive at the threshold, we first calculate the depth-dependent initial stresses on the fault. The depths we choose for illustration include the middle of each interval and the TOB shown in Fig. 2. From Sect. 2.3, we start with an in-situ effective

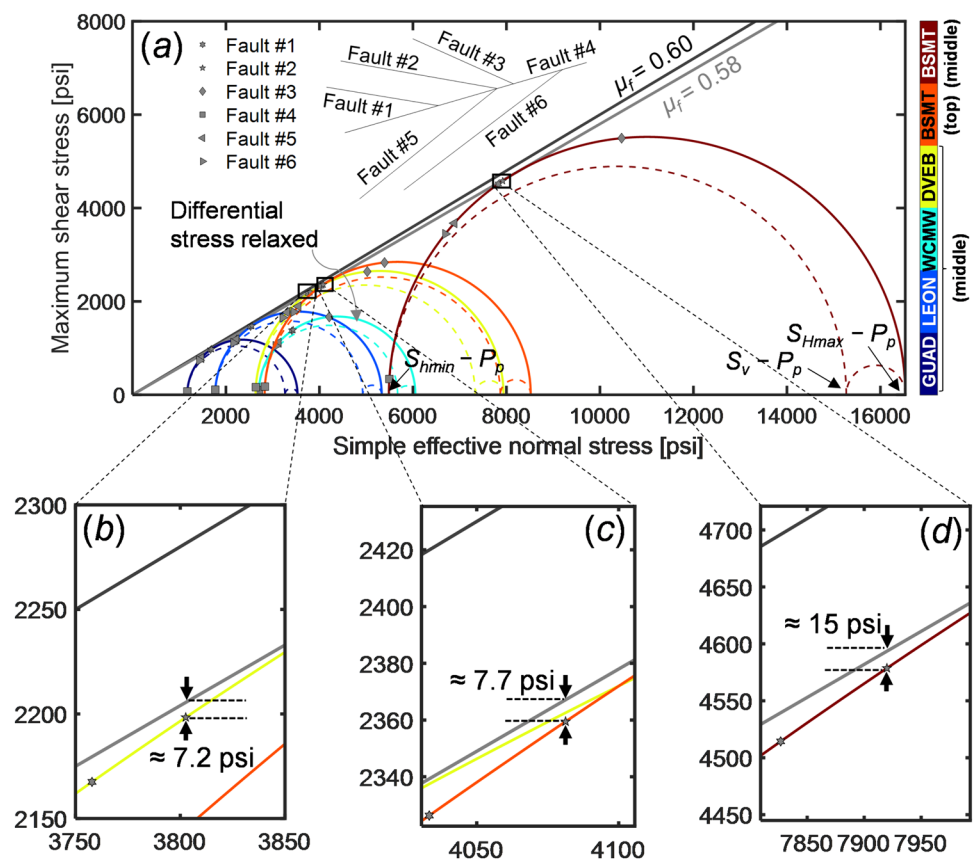
stress tensor obtained following the Terzaghi effective stress law appropriate also for faults (Jaeger and Cook 1979). We use it to calculate first the initial effective normal stress and maximum shear stress resolved the fault and then the initial CFF following procedures detailed in Sect. 3.2. We repeat the steps for all faults at all depths, and the results are illustrated in the Mohr space, see Fig. 5a. Faults are represented as points, and the six sets of 3D Mohr circles correspond to the six chosen depths. Because the faults are vertical (i.e., parallel to S_v), they always fall onto the largest Mohr circles defined by S_{Hmax} and S_{hmin} . The main shear failure envelope defined by $\mu_f=0.58$ is shown in grey, and a complete list of the initial CFF on each fault at all chosen depths is provided in Appendix A.2. An envelope associated with $\mu_f=0.6$ is also shown in black for reference. The triggering threshold is simply the absolute value of the initial CFF, that is, the vertical distance between the point representing a fault and the main failure line, independent from subsequent stress paths toward failure. A few points are worth noting. First, excluding the WCMW, the triggering threshold tends to increase with depth. This will prove useful in constraining the upper extents of faults using modeled CFF changes at shallower depths, to be detailed in Sect. 4. Second, within the WCMW itself, the triggering threshold is much higher than in other intervals, due to relaxed differential stress and increased stress isotropy. This means that shales with time-dependent behaviors can act as a barrier to not only hydraulic fracturing (Xu et al. 2019) but also seismicity. Third, fault #2 is the most critically stressed of all. Figure 5b–d provide close-up views of fault #2 in the Mohr space at three key depths: within the DVEB, and at the top and middle of the basement. The associated triggering thresholds are around 7.2 psi, 7.7 psi, and 15 psi, respectively.

3 Methods

3.1 Fully Coupled Hydro-Mechanical Numerical Modeling

As was introduced in Sect. 1, we implement a general poromechanical framework in 3D using Abaqus following the methodology documented in Jin (2023) and procedures established in Jin et al. (2023). Here, we summarize several key points. The set of fully coupled mass balance law for the pore fluid and quasi-static force balance law for the fluid-saturated porous rock is a generalization of Biot poroelasticity (Biot 1941; Rice and Cleary 1976) and naturally gives rise to 1st- and 2nd-orders of fluid–solid full coupling. Biot poroelasticity postulates the 1st-order monolithic coupling in that the volumetric strain rate of the porous solid skeleton acts as an equivalent fluid source, and the negative pore pressure gradient acts as an equivalent body force (Wang 2000;

Fig. 5 Initial stresses visualized in the Mohr space. **a** Six sets of 3D Mohr circles colored by depths together with fault-representing points shaped by fault indices. The main failure line ($\mu_f=0.58$) is in grey and a reference failure line ($\mu_f=0.60$) is in black. **b–d** The criticality of fault #2 illustrated by its initial stress state at three depths: within the DVEB and at the top and middle of the basement. At each depth, the earthquake-triggering threshold as the vertical distance between the fault and the main failure line is indicated (Color figure online)



Segall 2010). In our framework, the 1st-order coupling is similar, and the 2nd-order coupling arises from additional incremental pore volume changes as a function of the pore pressure and solid particle velocity. While the 2nd-order fluid-to-solid coupling is always present due to changes in mixture densities, the 2nd-order solid-to-fluid coupling persists only when the solid particle velocity is non-orthogonal to the Darcy velocity and vanishes otherwise. In terms of constitutive laws, macroscopically, we implement the linear Darcy's flow for the pore fluid and the linear generalized Hooke's law for the porous solid, and microscopically, we consider linear compression of the fluid as a function of pore pressure, and linear compression of solid grains and pores as functions of pore pressure and mean effective stress, where the latter was derived by Coussy (2004). Fluid injection is modeled using direct mass rate source terms prescribed at the nearest available free nodes, as opposed to more representative but expensive line source terms prescribed at explicitly modeled and meshed wells (Chang and Yoon 2022; Haddad and Eichhubl 2023). All governing equations are formulated using injection-induced perturbing quantities only, and the boundary and initial conditions are prescribed accordingly. We use a two-field mixed finite element method for fully coupled space discretization and a

backward Euler method for fully implicit time stepping. A comprehensive theoretical description of this algorithm can be found in, e.g., Jin and Zoback (2017). Finally, because we model all intervals including the low-permeability WCMW as poroelastic layers, the problem partially approaches the undrained limit, and the discretized fully coupled equations become numerically unstable when solved using equal-order interpolations (Murad and Loula 1994). To circumvent this issue, we instead employ first-order interpolations for the pore pressure and 2nd-order interpolations for the displacements to suppress spurious pore pressure oscillations, using the so-called Taylor–Hood family of finite elements (Hughes 2012; White and Borja 2008). All these procedures can be achieved following the Abaqus user manual (Dassault Systèmes Simulia 2014). Recently, the numerical solutions to Abaqus's poromechanical framework have been validated against the classic Rudnicki (1986) analytical solutions and demonstrated robust for point-source constant-rate injection within a homogenous and isotropic full space, and the general framework has been adopted and implemented in other induced seismicity studies (Hill et al. 2023, 2024).

The mesh consists of over 2 million finite elements with nearly 1 million nodes representing the six intervals, see Fig. 6. Faults are built explicitly, with two representative

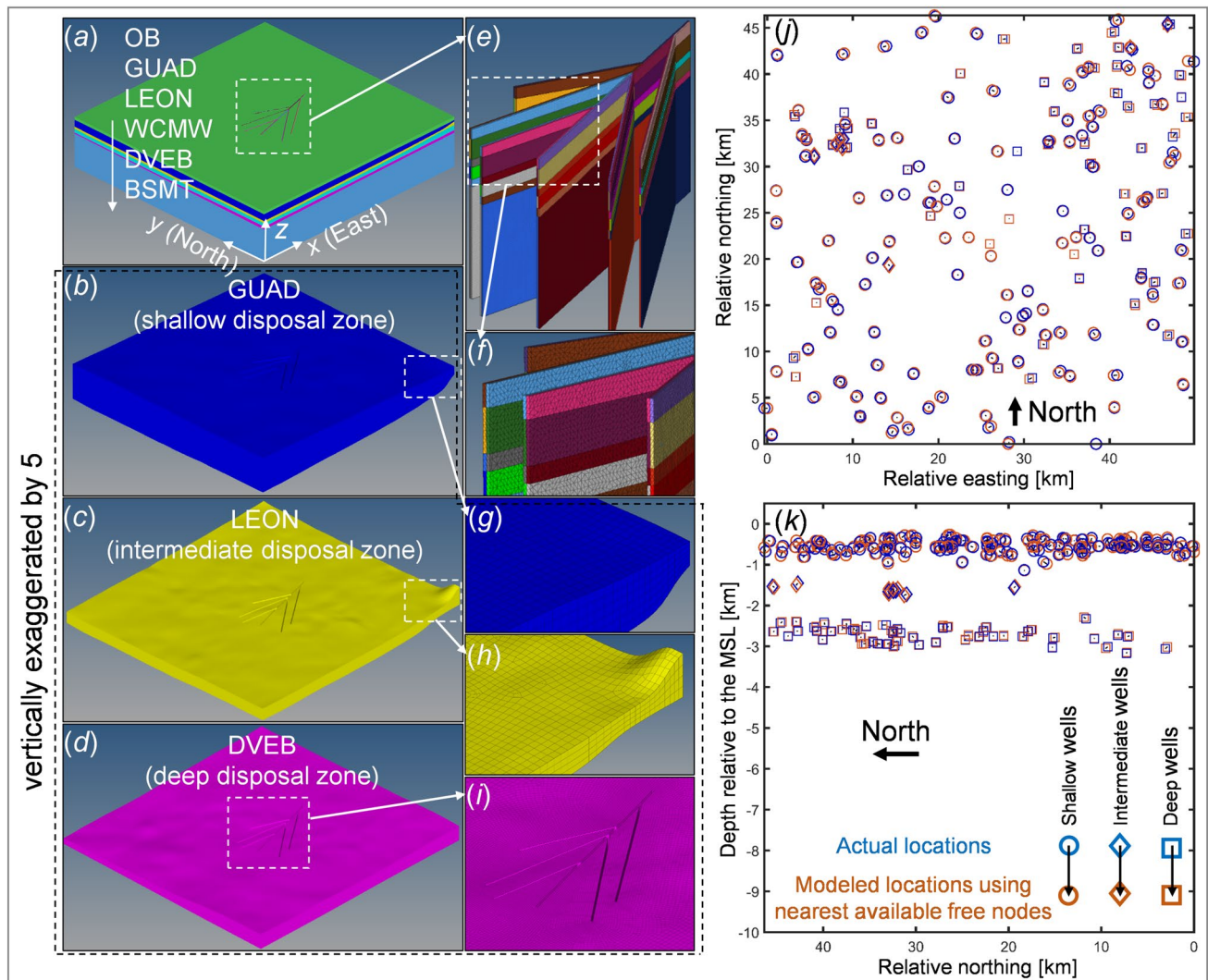


Fig. 6 3D finite element mesh of the entire faulted domain **a**, the shallow, intermediate, and deep disposal intervals **b–d**, and the fault zone **e**. Close-up views are shown for four selected regions within the white-dash boxes **f–i**. To show the surface topography of the formation tops, a vertical exaggeration factor of 5 is applied **b–d**, **g–i**.

fault-zone structures (see Sect. 3.4) intersecting all intervals. To model various upper extents of faults, fault segments within a certain interval are turned on and off by assigning properties of either the faults themselves or the surrounding rock. Surface topographies of all intervals are strictly preserved during meshing. The model parameters are jointly derived from log data and the literature, as listed in Jin et al. (2023). Notably, the permeability we use for the Ellenburger is on the order of 10^{-14} m²/s, which agrees with independent estimates constrained by surface deformation (Shirzaei et al. 2019) and seismicity onset (Tung et al. 2021).

The modeled well locations (orange dots) using the nearest available free nodes and calibrated against actual well locations (blue dots) are shown in map view **j** and west side view **k**, with errors shown as the connecting black arrows (Color figure online)

3.2 Stress Tensor Rotation and Superposition and Coulomb Stress Change Calculation

For subsequent analysis, we rotate the in-situ stresses described in Sect. 2.3 from the principal coordinate system \underline{x} into the model's Cartesian coordinate system \underline{x} , see Fig. 6a. This is done as $\underline{S} = \underline{A}\underline{S}\underline{A}^T$, where \underline{S} and \underline{S} are the same stress tensor described in \underline{x} and \underline{x} , respectively, and \underline{A} is the standard rotational matrix consisting of directional cosines (Zoback 2010). The two horizontal stresses, S_{hmin} and S_{hmax} , are thus transformed into $S_{xx} = 1.0702$ psi/ft, $S_{yy} = 0.8055$, and $S_{xy} = 0.0962$ psi/ft within the WCMW, and $S_{xx} = 1.0725$ psi/ft, $S_{yy} = 0.7035$, and $S_{xy} = 0.1340$ psi/ft in the remaining intervals. The vertical component

remains unchanged. Following a compression positive sign convention, the in-situ simple effective stress tensor σ'_0 can now be easily obtained as $\sigma'_0 = \mathbf{S} - P_p \mathbf{1}$, where $\mathbf{1}$ is the Kronecker delta. The final simple effective stress tensor σ'_1 is obtained through superposition as

$$\sigma'_1(x, t) = \sigma'_0(x) + \sigma'(x, t) \quad (1)$$

Here, $\sigma'(x, t)$ is the perturbing simple effective stress tensor calculated according to the traction continuity condition across an arbitrary fault (Jin 2022)

$$\sigma'(x, t) = \tilde{\sigma}'(x, t) + \alpha p(x, t) \mathbf{1} - p(x, t) \mathbf{1} \quad (2)$$

where α is the effective stress coefficient (Borja 2006), which equals to the widely known Biot coefficient, and $\tilde{\sigma}'$ and p are the perturbing effective stress tensor and pore pressure of the hosting rock, both used in formulating the governing laws and solved for numerically (Sect. 3.1).

Finally, we compute ΔCFF (i.e., changes in CFF), which will be compared against the triggering thresholds discussed in Sect. 2.3 to understand seismicity onset. A common practice is to directly compute changes in the effective normal stress and maximum shear stress from σ' for ΔCFF without considering σ'_0 (e.g., Barbour et al. 2017). This approach is not favored as the maximum shear stress generated by σ' is not necessarily aligned with the initial maximum shear stress from σ'_0 . Here, we compute the change in CFF as

$$\Delta\text{CFF} = \text{CFF}_1 - \text{CFF}_0 \quad (3)$$

Here,

$$\text{CFF}_j = \left[\|\sigma'_j \cdot \mathbf{n}_f\|^2 - (\sigma'_j \cdot \mathbf{n}_f \cdot \mathbf{n}_f)^2 \right]^{\frac{1}{2}} - \mu_f (\sigma'_j \cdot \mathbf{n}_f \cdot \mathbf{n}_f), \quad j = 0, 1 \quad (4)$$

where \mathbf{n}_f is the unit normal vector to a fault plane of interest, and CFF_0 and CFF_1 are the in-situ Coulomb stress and the final perturbed Coulomb stresses, respectively.

3.3 Coulomb Faulting Analysis and Rate-and-State Earthquake Rate Modeling

We perform Coulomb faulting analysis to understand seismicity onset and distribution. To this end, we first identify based on Sect. 2.4 the critical ΔCFF required to meet the triggering threshold and then track its evolution. We assume instantaneous earthquake nucleation upon the arrival of the critical ΔCFF on seismogenic fault #2 and calibrate the arrival time against the mainshock origin time and the distribution against event locations.

To identify potential nucleation effects and further understand seismicity distribution, we also implement the Dieterich (1994) earthquake nucleation and production constitutive model.

The model is originally derived for an elastic rock embedded with ubiquitous and non-interacting rate-and-state frictional seismogenic sources and maps the stressing rate into a seismicity rate via the following homogeneous, nonlinear, and 1st-order ordinary differential equation

$$\frac{d}{dt}R(t) = -\frac{1}{t_a}R(t)^2 + \frac{1}{t_a} \frac{\dot{\tau}(t)}{\dot{\tau}_0}R(t) \quad (5)$$

where t is the time, d/dt is the total time derivative, R is the seismicity rate relative to the background rate, $\dot{\tau}_0$ is the background stressing rate assumed to be always greater than 0, $\dot{\tau}$ is the Coulomb stressing rate, and t_a is a characteristic decay time that reads

$$t_a = a \frac{\bar{\sigma}}{\dot{\tau}_0} \quad (6)$$

Here, a is a constitutive parameter characterizing the rapid response of fault friction to a step-up in the sliding velocity (e.g., Segall 2010) and $\bar{\sigma}$ is recast by Segall and Lu (2015) for a poroelastic medium as the background simple effective normal stress resolved on the seismogenic fault.

In this study, we conduct seismicity rate modeling only for seismogenic fault #2. We set $\dot{\tau}_0$ to a typical 0.001 MPa/year (Segall and Lu 2015; Chang and Segall 2016), and a to 0.005 and 0.015, respectively, which roughly agree with the lower and upper bounds as measured on samples from the Permian Basin (Bolton et al. 2023); we approximate $\dot{\tau}$ numerically from the ΔCFF time series as $\dot{\tau}^{(k+1)} = (\Delta\text{CFF}^{(k+1)} - \Delta\text{CFF}^{(k)}) / (t^{(k+1)} - t^{(k)})$, where k indicates the time step, without first smoothing the ΔCFF as is sometimes done (e.g., Chang and Segall 2016); we calculate $\bar{\sigma}$ as $\sigma'_0 \cdot \mathbf{n}_f \cdot \mathbf{n}_f$ (see the second part of Eq. (4)); finally, we numerically solve Eq. (5) using the explicit high-order Runge–Kutta method.

3.4 Fault Scenario Testing

We model two representative fault-zone structures. In the first, a fault zone consists of highly permeable fault damage zones (FDZs) on both sides; in the second, a nearly impermeable fault gouge zone (FGZ) is sandwiched between the two FDZs. The FDZs are represented using equal-dimensional elements and discretized explicitly in the model, whereas the FGZs are modeled as split nodes subject to displacement continuity constraints while permitting pore pressure discontinuities. Due to their vertical and strike-slip nature, the upper extents of faults are uncertain. Here, we test three fault vertical extents. In the first, the faults cut through all intervals; in the second, the faults are rooted in the basement and extend into the overlying DVEB; in the last, the faults are restricted to within the basement and terminate at the TOB. Combining fault-zone structures and fault extent leads to six scenarios, namely scenarios 1a, 1b,

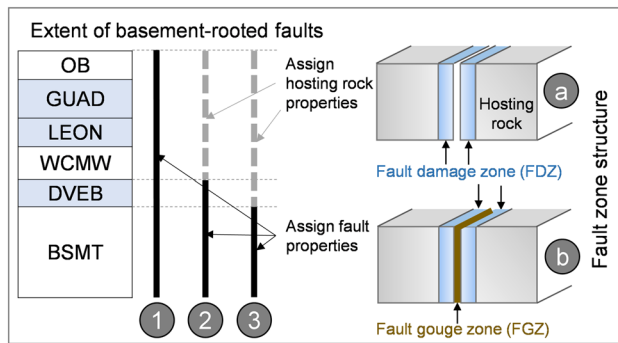


Fig. 7 Six fault scenarios tested in the study, resulting from three fault upper extents labeled with 1, 2, and 3, and two fault-zone structures labeled with a and b. The six intervals are also shown for reference, with the three disposal intervals highlighted. The meshing is done once for all, but fault segments in different intervals are allowed to have different properties to mimic varying fault upper extents (see Sect. 3.1)

2a, 2b, 3a, and 3b, see Fig. 7. The geometric and hydro-mechanical parameters of the fault zones are also detailed in Jin et al. (2023).

From a seismicity triggering perspective, common among the scenarios is that any given injection zone imparts out-of-zone poroelastic stress to all remaining intervals including the basement; the difference lies in the vertical pore pressure transfer. The basement draws pore pressure from all disposal intervals in scenarios 1a and 1b but only from the deep disposal interval in scenarios 2a and 2b. Scenarios 3a and 3b represent a transition from hydraulic connection to hydraulic disconnection between the deep disposal interval and the basement. Some studies assume the configuration in these two scenarios (e.g., Zhai et al. 2021) is representative for induced seismicity analysis. Strictly speaking, the deep disposal interval still imparts fluid flux and thus pressure to the basement, albeit only through the transversal width of the FDZs at the TOB.

4 Results and Discussion

4.1 Scenarios 1a and 1b: Faults Cutting Through All Intervals

Scenarios 1a and 1b have been modeled in Jin et al. (2023). There, we documented the four-decadal evolution of pore pressure and poroelastic stress changes within all intervals across depths, characterized cross-interval interactions, and quantified the effects of shallow and deep injections on basement stressing. Here, we continue by analyzing the faults. Following procedures detailed in Sect. 3.2, we compute and record the ΔCFF at all fault element centroids. In scenario 1a, this is done only for the FDZ on either side, since the

pore pressure and stresses are continuous across the FGZ; in scenario 1b, however, this is done for the FDZs on both sides due to discontinuities in the pore pressure, and resultantly, the effective stress tensor and the Coulomb stress. The distribution of ΔCFF around the onset of the investigated sequence (January 2021) is shown on all faults in 3D view and on seismogenic fault #2 in 2D side view in Appendix A.3, see Fig. 19. The time series of ΔCFF at all locations on fault #2 are plotted from January 2015 to April 2021, see Fig. 8. The results are separated based on the hosting intervals from the GUAD to the BSMT, and displayed for the FDZ on either side in scenario 1a (Fig. 8a–e) and for the FDZs on both sides in scenario 1b (Fig. 8f–j, Fig. 8k–o). The control of fault-zone structure on fault stress is evident. The depth-varying earthquake-triggering thresholds as discussed in Sect. 2.4 and listed in Table 1 are indicated. The earthquakes within the investigated sequence (Fig. 1c) are disaggregated and attributed back to their respective hosting intervals, and their magnitudes over the same period are plotted. Finally, injection rates within all three disposal intervals are superposed for reference in the left column of the figures. Here, the triple-zone injection collectively induced Coulomb stress changes on fault #2 by -10 – 20 psi. A negative ΔCFF is uniquely characteristic of poroelastic stressing and cannot be captured by modeling pore pressure diffusion only. Depending on the configuration, the injection can sometimes stabilize a fault (Segall and Lu 2015; Juanes et al. 2016). An example is captured in Fig. 19, where well #23 reduced the CFF on the segment within the GUAD. The ΔCFF time series within each disposal interval largely coincide with in-zone injection rates, and the last episode of CFF increase, seen in all intervals, coincides with the main earthquake sequence. The segment within the WCMW experienced the most prominent changes, but because of the increased stress isotropy (Fig. 4) and elevated triggering threshold (Fig. 5a), it remained uncritically stressed. Overall, the shallower segments experienced more changes than the deeper segments while requiring fewer CFF increases to be activated. These results suggest that seismicity would have occurred at shallower depths (i.e., within the GUAD and LEON) and much sooner (i.e., between 2016 and 2017). The absence of these observations suggests the implausibility of these two scenarios.

4.2 Scenarios 2a and 2b: Basement-Rooted Faults Extending into the Deep Disposal Interval

4.2.1 One Critical Depth and Two Periods

To understand seismicity triggering in scenarios 2a and 2b, we must first infer a critical depth at which the earthquake sequence was most likely initiated. Here, shallower intervals (i.e., above the DVEB) are unlikely to be seismogenic for three reasons.

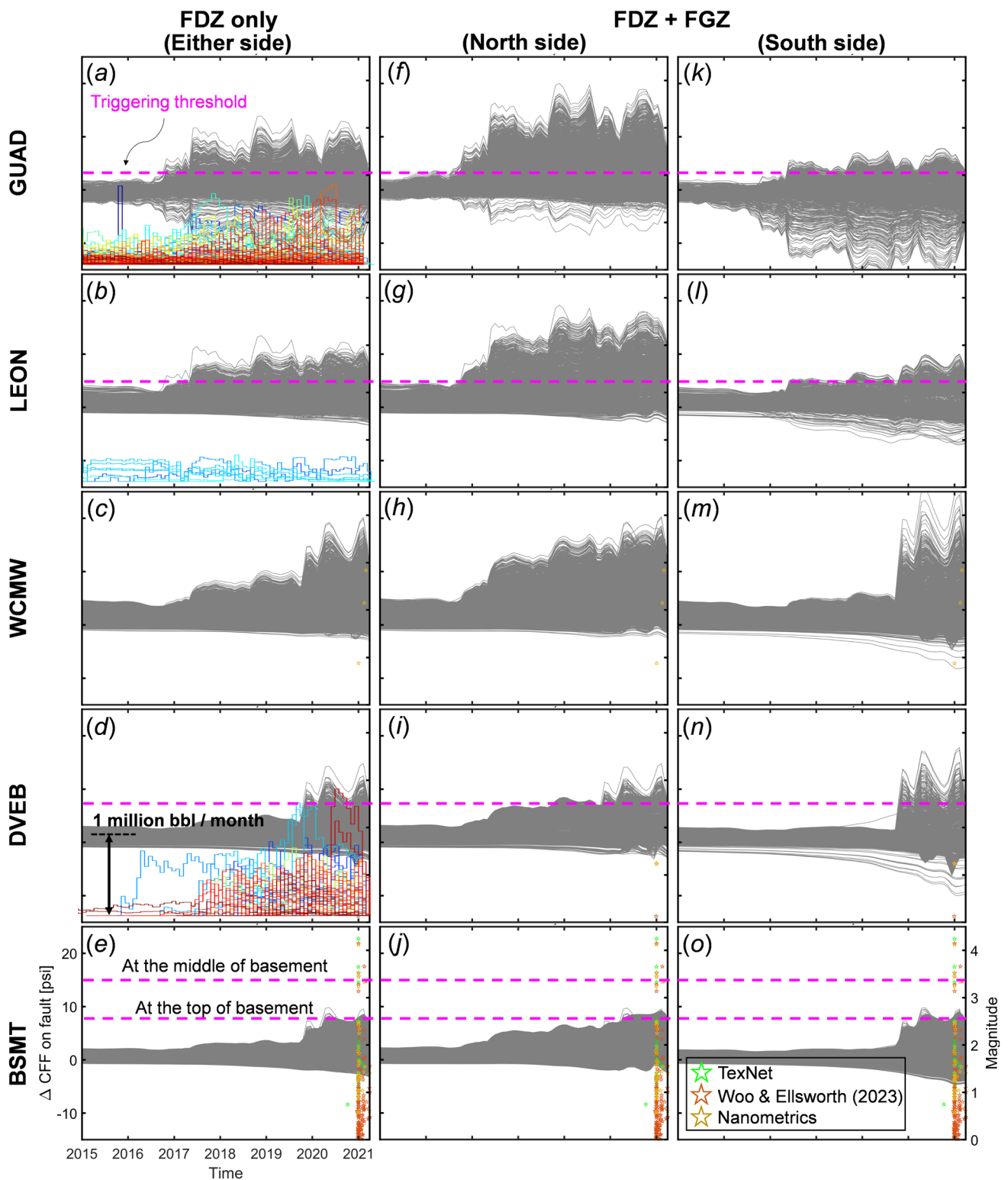


Fig. 8 Modeled CFF changes over time at all element centroids on fault #2 from January 2015 to April 2021. The rows correspond to fault segments from shallow to deep, hosted within the GUAD, LEON, WCMW, DVEB, and BSMT, respectively. **a–e** Results on either side of the fault in scenario 1a. **f–j** and **k–o** Results on the two sides of the fault in scenario 1b. The North and South sides are illustrated in Fig. 19. Events in the main earthquake sequence are plot-

ted over the same period with their magnitudes shown by the y-axis on the right. The dashed magenta lines indicate the associated earthquake-triggering threshold for fault #2, see also Fig. 5 and Table 1, and are out of the displayed range for the WCMW. The injection rates shown in Fig. 3 are superposed for reference and colored by operators. Both events and injection rates are separated according to the hosting intervals

Table 1 Initial CFF [psi] on faults at the middle depth of each interval assuming $\mu_f=0.58$

	Fault #1	Fault #2	Fault #3	Fault #4	Fault #5	Fault #6
GUAD	-5.4	-3.2	-122.3	-608.8	-68.1	-93.2
LEON	-8.1	-4.8	-184.7	-919.3	-102.8	-140.7
WCMW	-607.0	-603.8	-773.2	-1464.4	-696.0	-731.7
DVEB	-12.1	-7.2	-274.9	-1368.3	-153.0	-209.4
BSMT (Top)	-12.9	-7.7	-295.1	-1468.6	-164.2	-224.7
BSMT (Middle)	-25.1	-14.9	-572.6	-2849.8	-318.6	-436.0

First, the faults (i.e., seismogenic sources) are simply absent. Second, creating a fresh fault by breaking the intact hosting rock in shear failure mode requires a much higher CFF increase. For instance, the earthquake-triggering threshold increases by nearly 150 psi from typical rock cohesion of 1 MPa alone, and by even more from internal friction. This value is too high and tends to be ruled out by the modeled ranges of CFF increases in shallower zones (Jin et al. 2023). There, using a fault-free scenario, we demonstrated that the CFF increases in the GUAD and LEON peaked merely at around 25 psi. Third, the WCMW is far from failure due to unfavorable stresses. Meanwhile, by directly hosting the deep injection, the DVEB experiences a higher Coulomb stress increase and simultaneously requires a lower triggering threshold than the basement. Combining all these, we infer that the earthquake sequence was initiated from within the DVEB.

We now explore the plausibility of these two scenarios by examining whether they reproduce triggering processes that hindcast seismicity onset and explain seismicity distribution. To do so, we take a horizontal slice at the inferred earthquake initiation depth, specifically, the middle of the DVEB, and visualize the evolution of Δ CFF in map view. Since the earthquake-triggering threshold at this depth is around 7.2 psi, we shall highlight accordingly the critical Δ CFF required to meet this threshold using an iso-value contour. But considering uncertainties, we instead show a range of neighboring iso-value contours from 6 to 8 psi at a 0.25 psi increment. We partition the modeled period (January 1983–April 2021) into two parts: before and after the critical Δ CFF reaches the faults. The two scenarios are similar in the first part but differ in the second due to faults and fault-zone structures taking effect. In a loose sense, we illustrate using the first part contributions by historical and distal wells, and the second part, contributions by recent and proximal wells as well as effects of faults and fault-zone structures.

4.2.2 Historical Stressing

The results from the first part, shown for scenario 2a and are nearly identical for scenario 2b, are illustrated in Fig. 9a–j at chosen times sparsely spaced and spanning from 1990 to 2019. The Δ CFF, no more than 200

psi, is shown in color with the critical Δ CFF indicated by magenta contours. The in-zone wells (i.e., deep wells) and the out-of-zone wells (i.e., shallow wells, and intermediate wells) are illustrated in black and grey, respectively, and are sized and shaped the same as in Fig. 1b. The Δ CFF “plumes” are seen surrounding the deep wells and are also noticeable near the intermediate wells but hardly visible around the shallow wells. This means that, at this depth, the Δ CFF is predominantly due to the in-zone deep injection itself, with some contribution from the intermediate injection in the LEON and little contribution from the shallow injection in the GUAD. Identifying the subset of wells that potentially contributed to seismicity is completed in two steps: (1) track down the sources of the critical Δ CFF (i.e., wells that emitted magenta contours), and (2) check if the critical Δ CFF reached the seismogenic fault #2. For example, we identified two groups of wells that imparted 6–8 psi CFF increases near the left tip of fault #2 by June 2019. The first group contains all four intermediate wells to the Northwest, wells #48, #51, #54, and #55. Their perturbations are strong enough to be felt within the DVEB, due to persistent injection cumulating the largest volumes (Fig. 3). These perturbations have been propagating from afar toward fault #2 for decades (Fig. 9a–g), illustrating the possibility of a decades-long lag between injection and seismicity. In addition, this group also contains several deep wells, such as wells #22, #38, #49, #50, #95, and #131. These wells, all started injecting after 2016, produced critical Δ CFF that coalesced with and accelerated the propagation of that generated by the intermediate wells (Fig. 9e–j). Therefore, the first group serves as an example of the collective effect of dual-zone injections. The second group includes only deep wells that are to the Northeast, most notably, well #183, the critical Δ CFF from which steadily advanced (Fig. 9a–h), merged with that of well #39 in 2019 (Fig. 9i), and accelerated toward the faults (Fig. 9j). Although some other deep wells to the East (e.g., wells #161, #177), the Southeast (e.g., well #28), and the Southwest (e.g., wells #41, #120, and #160) also generated critically high Δ CFF, the elapsed time was insufficient for them to reach the faults (Fig. 9g–j).

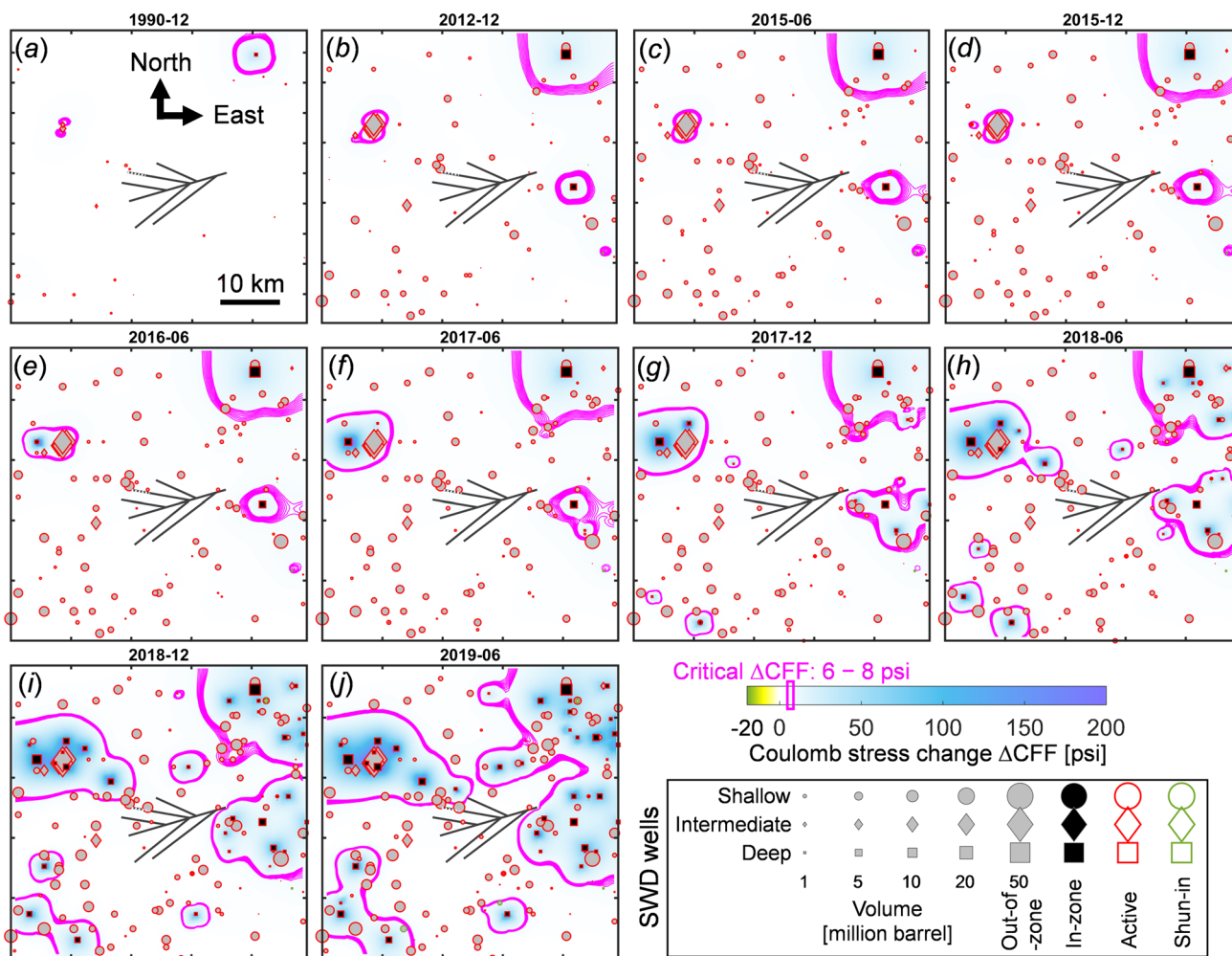


Fig. 9 Snapshots of modeled ΔCFF at the inferred earthquake initiation depth (i.e., within the DVEB) taken at 10 chosen times **a–j** from December 1990 to June 2019. Blue colors indicate CFF increases, and green colors, albeit absent in the results here, indicate CFF drops. The magenta lines are iso-value contours plotted from 6 to 8 psi at a 0.25 psi increment, sampling roughly ± 1 psi range around the earthquake-triggering threshold of 7.2 psi at this depth. SWD wells

are sized and shaped the same as before but are now shaded in black if in-zone and grey if out-of-zone. A well is highlighted with a red edge if it was still injecting and a green edge if it was shut in as of the time noted at the top of each subplot. The results, showing the period before faults took effect, are generated using scenario 2a and are nearly identical for scenario 2b (Color figure online)

4.2.3 Recent Stressing and Effects of Faults and Fault-Zone Structures

To illustrate the second part, we choose a 19.5 km by 12 km area surrounding the faults and the period between December 2019 and April 2021, which covers 1 year before and 4 months after the investigated sequence. Figure 10a–g display the results from scenario 2a at variably spaced times. Several new deep wells, e.g., wells #1, #2, and #11, started injecting over this period. The ΔCFF remained below 200 psi with local peaks spatially coinciding with only deep wells, demonstrating again the minimal effect of shallow SWD. We now highlight several processes potentially relevant to the subsequent seismicity triggering. First, the

historical critical ΔCFF from the first part continued propagating toward the center (Fig. 10a–c) until the shut-in of all wells (Fig. 10d), which took place following the investigated sequence in January 2021. For example, the portion jointly induced by intermediate and deep SWD and coming from the Northwest, and the portion driven by deep SWD and arriving from the Northeast, advanced noticeably before January 2021 but remained stagnant afterward; the deep SWD-driven portions arising on the East and the Southeast also appeared to be stalled near-fault #6 since the shut-in (Fig. 10e–g). Second, within the recent critical ΔCFF , the portion generated by well #11 merged with and accelerated the historical critical ΔCFF (Fig. 10a), whereas the portion produced by wells #1 and #2 acted independently, briefly

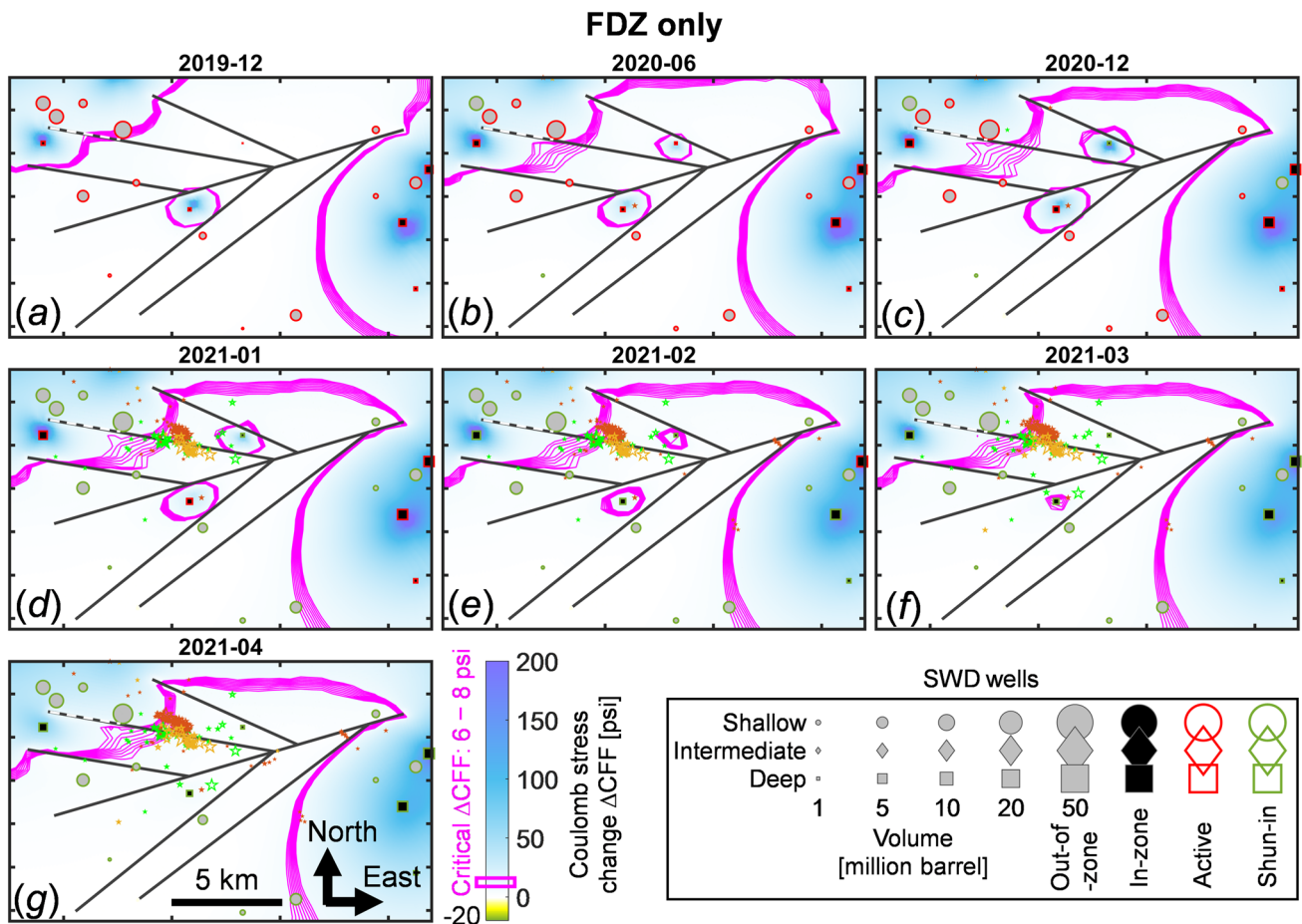


Fig. 10 Snapshots of modeled ΔCFF at the inferred earthquake initiation depth (i.e., within the DVEB) and near the faults in scenario 2a taken at seven chosen recent times from December 2019 to April 2021. The faults and fault-zone structures took effect over this period. **a–c** Before shut-in, **d** at the onset time of the investigated sequence, and **e–g** post-shut-in. Same as in Fig. 9, the colors illustrate ΔCFF , the magenta contours highlight a range of critical ΔCFF , and the cir-

cles and squares represent shallow and deep SWD wells, respectively, with the meaning of their shading and edge colors indicated. On each subplot, earthquake events that are within the investigated sequence and have occurred as of the associated time are shown using the same legends as in Fig. 1c, and the uncertain segment of fault #2 is marked with a dashed line

expanding before the shut-in (Fig. 10a–d) before receding afterward (Fig. 10e–g). Third, while the recent critical ΔCFF surrounding wells #1 and #2 retreated swiftly post-shut-in, the historical portions largely lingered (Fig. 10e–g) and were sustained by continuing injection in the far field. We infer that curtailing far-field injection may also help mitigate near-field seismicity, although detailed understanding requires further modeling.

Jin et al. (2023) illustrated that inside a disposal interval, faults act as pore pressure sinks to alleviate pressurization near them; faults also tend to reduce the vertical normal component, amplify the two lateral normal components, and redistribute all three shear components of the simple effective stress tensor, due to an inward- and downward-pointing negative pore pressure gradient field that scales linearly with the flow velocity field. As a result, faults modulate the propagation of the critical ΔCFF , albeit differently depending

on the fault orientation, see Eqs. (3) and (4). For instance, before the shut-in, the portion arriving from the Northwest became dispersed after reaching faults #1–#3 (Fig. 10b–d), whereas the portion coming from the East concentrated near the northeast segments of faults #4 and #6 (Fig. 10a–d). Faults #4 and #5 appeared to have contained the critical ΔCFF emitted by well #2 (Fig. 10a–c), likely resulting from the downward diversion of fluids.

The same snapshots from scenario 2b are shown in Fig. 11a–g, which when compared with Fig. 10a–g, elucidate a two-fold effect of fault-zone structures. First, the presence of the FGZs led to additional stress perturbations surrounding the faults, generating also negative ΔCFF by several psi (area in yellow) previously not observed in scenario 1a. Because the ΔCFF is calculated using the orientation of fault #2, its positive and negative changes directly indicate destabilizing and stabilizing effects on

cles and squares represent shallow and deep SWD wells, respectively, with the meaning of their shading and edge colors indicated. On each subplot, earthquake events that are within the investigated sequence and have occurred as of the associated time are shown using the same legends as in Fig. 1c, and the uncertain segment of fault #2 is marked with a dashed line

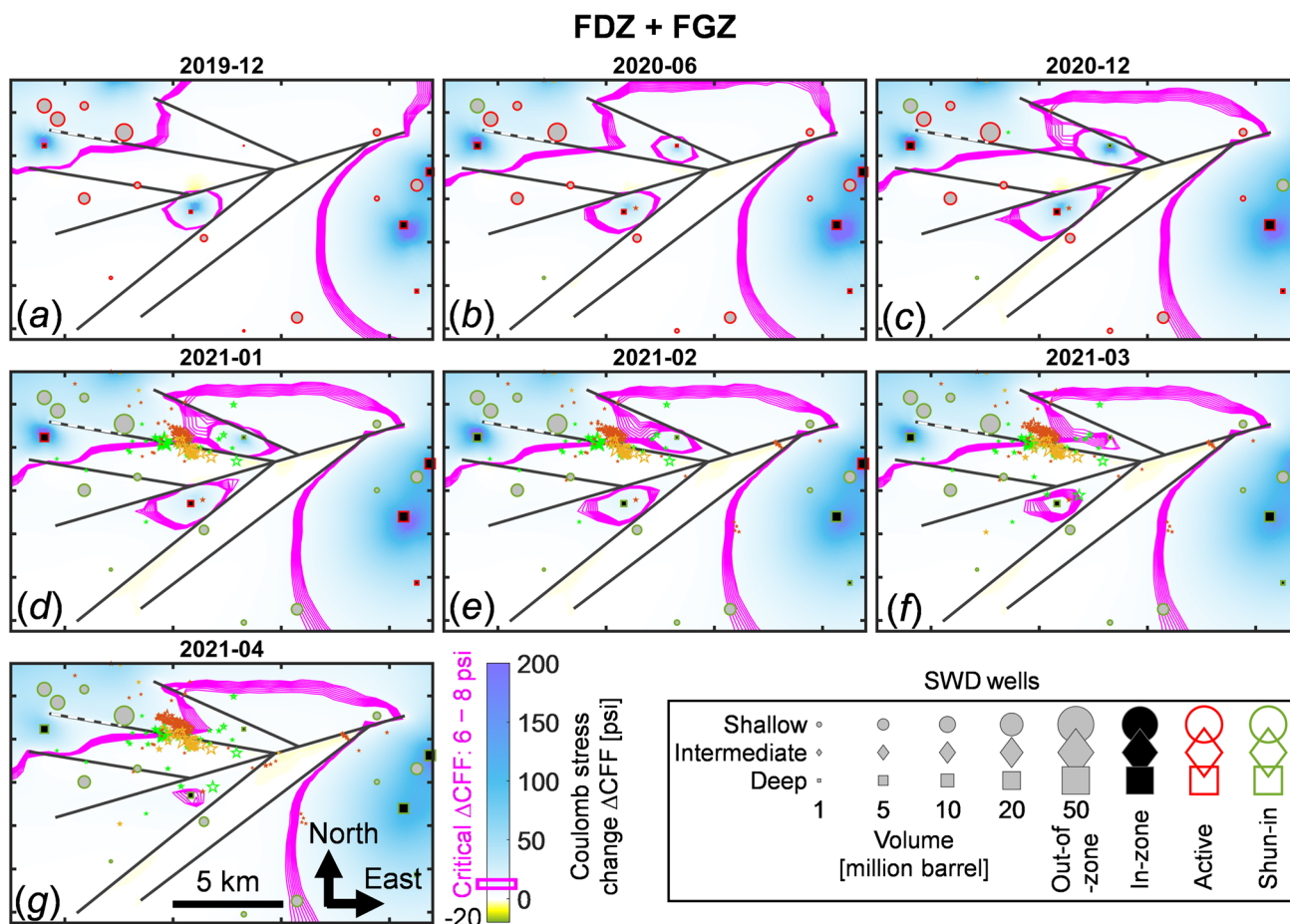


Fig. 11 Snapshots of modeled ΔCFF at the inferred earthquake initiation depth from within the DVEB and near the faults in scenario 2b taken at the same seven chosen recent times **a–g**, illustrating that

fault #2 and its parallel planes. For example, the Southeast tip of fault #2 experienced a reduction in ΔCFF , albeit trivially, and therefore was slightly stabilized (Fig. 11d–g). Second, while the differences in the ΔCFF itself due to FGZs are difficult to discern (the perturbing signals are small compared to the overall ΔCFF), the FGZ-induced amplification effect on the critical ΔCFF jacked between two neighboring faults is striking along the fault-tangential directions. For example, the historical critical ΔCFF coming from the Northwest and the recent critical ΔCFF produced by wells #1, both propagating between faults #2 and #3, were considerably stretched along the northwest-southeast direction (Fig. 11a–b), leading to their coalescence and a burst in the fault-destabilizing stress before the shut-in (Fig. 11c–d); similarly and over the same period, the recent critical ΔCFF emitted from wells #2 sandwiched between faults #4 and #5 dilated along the Southwest—Northeast direction. The amplification effect

the FGZs tend to amplify the critical ΔCFF tangentially between two bounding faults when compared to scenario 2a

also led to a slower retreat of the critical ΔCFF by wells #1 and #2 post-shut-in.

4.2.4 Seismicity Onset

In Sect. 4.2.3, we progressively added events that had occurred at a chosen time. For a scenario to be plausible within the Coulomb faulting framework, it first needs to be able to hindcast the onset of seismicity. Figure 18b shows that the onset of the sequence (i.e., time of the mainshocks) was in January 2021, consistent among all three catalogs. Therefore, in a plausible scenario, the critical ΔCFF at the earthquake initiation depth would have reached the epicentral locations of the mainshocks in January 2021. Scenario 2a successfully replicated such a moment, see Fig. 10d, where the portion of the critical ΔCFF arriving from the Northwest and intersecting fault #2 matches best with the mainshocks in the TexNet (2021) catalog and reasonably

well with those in the Woo and Ellsworth (2023) catalog. In addition, the portion generated by well #1 reached the Southeast segment of fault #2 and this agrees with several events from TexNet (2021) catalog. Scenario 2b yields an even better result, see Fig. 11d, where the critical Δ CFF coalesced, as explained above, and swept through the entire seismogenic segment of fault #2, matching excellently with all three catalogs. Hence, we argue that both scenarios are plausible, but scenario 2b is preferred. The previous detailed analysis of the two-stage stressing processes now allows us to trace the relevant portions of the critical Δ CFF back to their origins. As modeled, the source stressors include (1) the two groups of distal wells, with the first group consisting of both intermediate and deep wells and the second group

containing deep wells only (Sect. 4.2.2), and (2) two proximal and deep wells, wells #1 and #11 (Sect. 4.2.3). The roles of the immediately adjacent deep well #2 and all shallow wells are trivial.

4.2.5 Seismicity Distribution

We further test the plausibility of scenarios 2a and 2b by their ability to explain seismicity distribution. We first show the evolution of the final Coulomb stress (i.e., CFF_1) on fault #2 through three key times: (1) the critical Δ CFF arrival time in December 2019 (Fig. 10a, Fig. 11a), (2) the seismicity onset time in January 2021 (Fig. 10d, Fig. 11d), and (3) the halftime in June 2020 (Fig. 10b, Fig. 11b). The

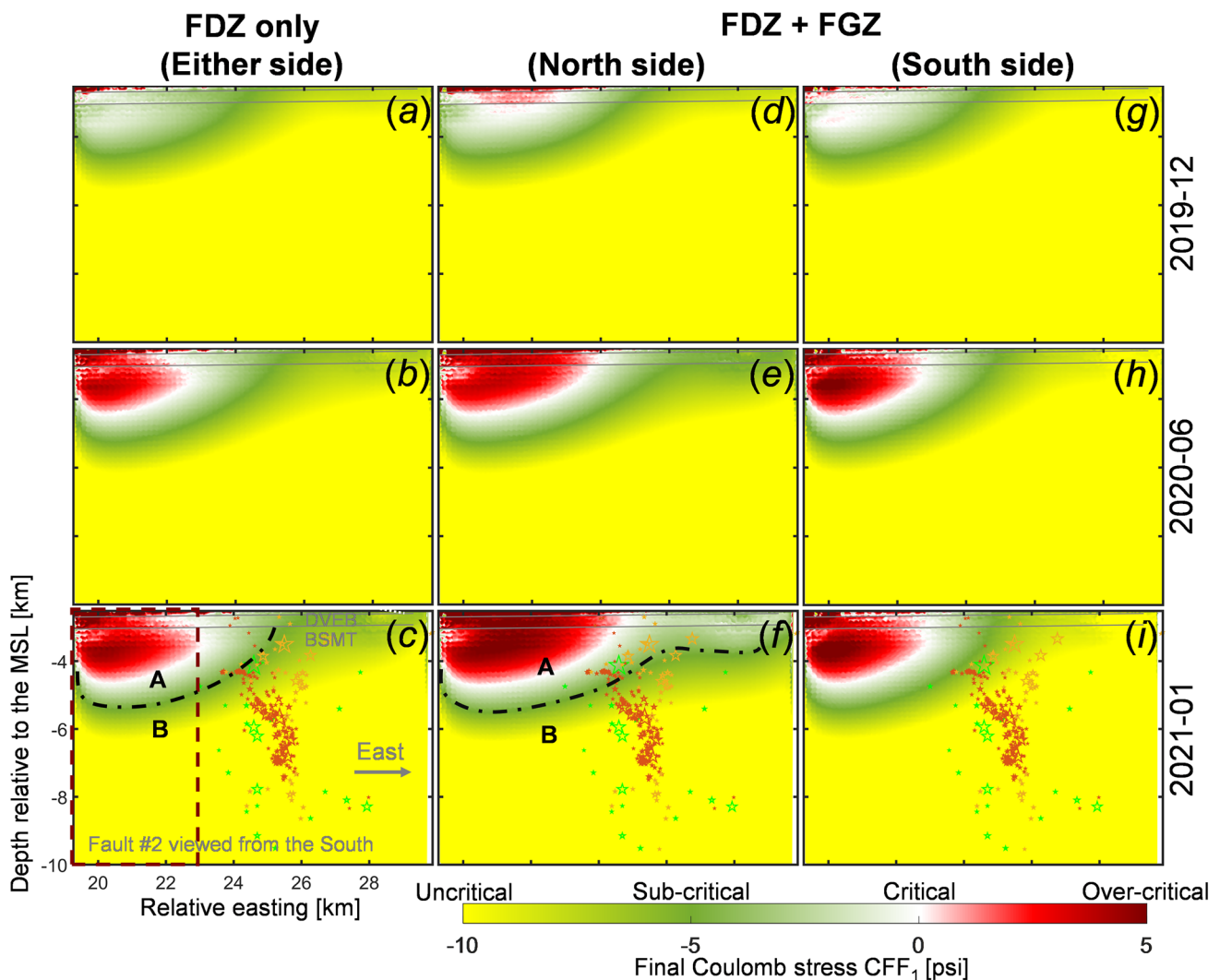


Fig. 12 North-facing snapshots of CFF_1 on fault #2 taken at three key times, see texts, for scenario 2a **a–c** and scenario 2b Northside **d–f** and Southside **g–i**. The fault only has segments within the DVEB and the basement in the two scenarios. Seismicity is shown at the onset time in January 2021. The over-critical, critical, sub-critical, and non-

critical portions are indicated in red, white, green, and yellow, respectively. The former three are amalgamated to form a near-critical patch A, separated by a black dash-dotted line from the remaining uncritical patch B. The uncertain segment of fault #2 is indicated with a dashed box in dark red (Color figure online)

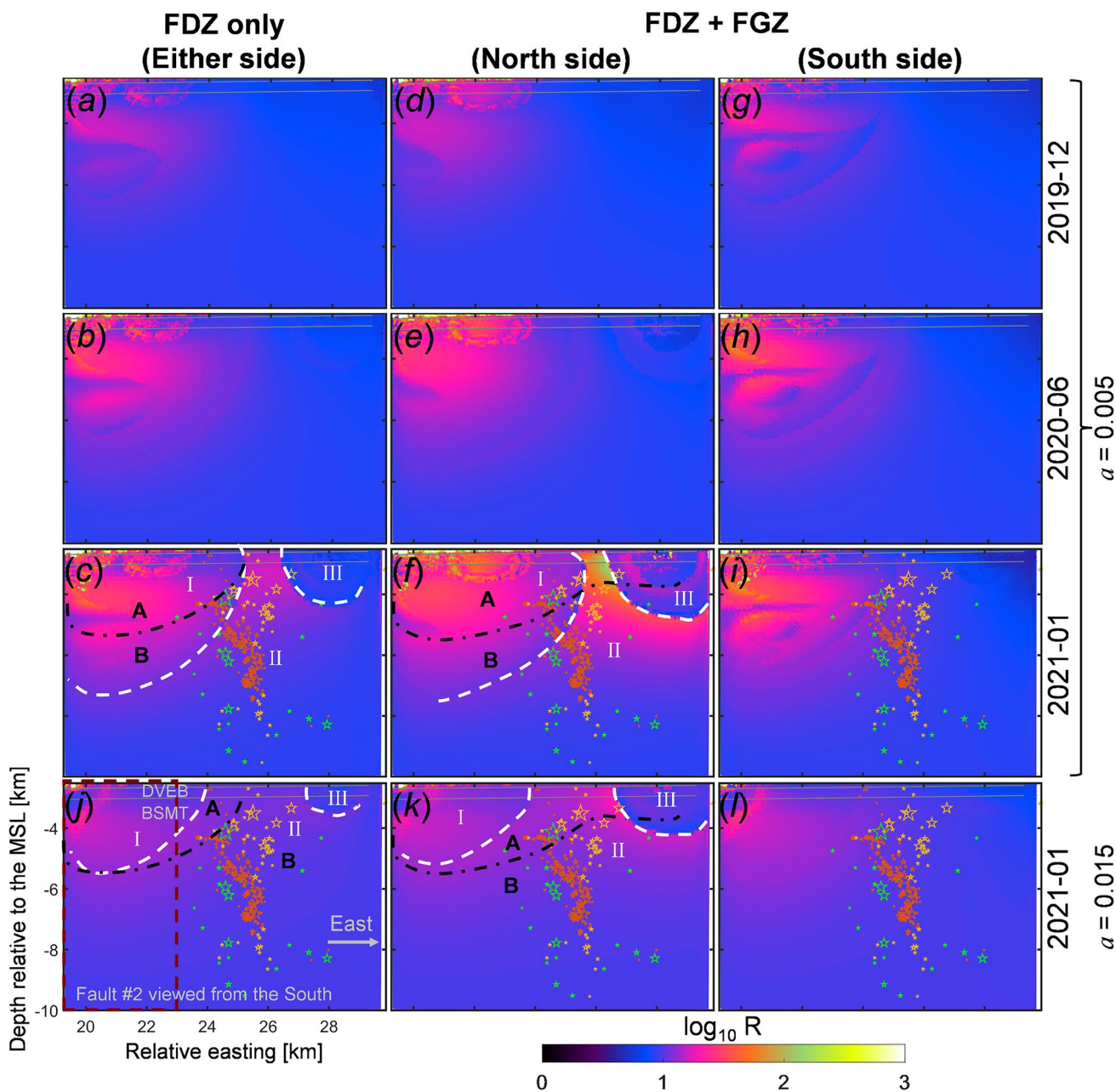


Fig. 13 North-facing snapshots of logarithmic-scale relative seismicity rate on fault #2 taken at three key times, see texts, for scenario 2a **a–c** and scenario 2b Northside **d–f** and Southside **g–i**, using an a value of 0.005. **j–l** Repeated at the seismicity onset time using an a value of 0.015. By January 2021, three distinctive patches had formed and were marked with white-dashed lines and labeled with I, II, and

III. Complementary patches A and B used in the Coulomb faulting analysis and plotted in Fig. 12 are also shown here for reference. The spatiotemporal evolution of patch II captures a probable nucleation process on fault #2, see texts, and explains seismicity outside patch A. The uncertain segment of fault #2 is indicated with a dashed box in dark red (Color figure online)

results are shown in the North-facing view in Fig. 12a–c for scenario 2a and Fig. 12d–i for scenario 2b distinguished between the two fault sides. The varying degree of criticality on the fault is indicated by colors, see the figure caption. We divide the fault into patches A and B, respectively, where the former experiences a near-critical (covering sub-critical

to over-critical) state whereas the latter remains uncritical, see Fig. 12c, f. Displaying CFF_1 distributions at the two earlier times will also prove useful in the next Section. At the onset time, we overlay the aggregated catalog, see Fig. 12c, f, and i. In the Coulomb faulting framework, seismicity is expected to spatially coincide with the near-critical fault

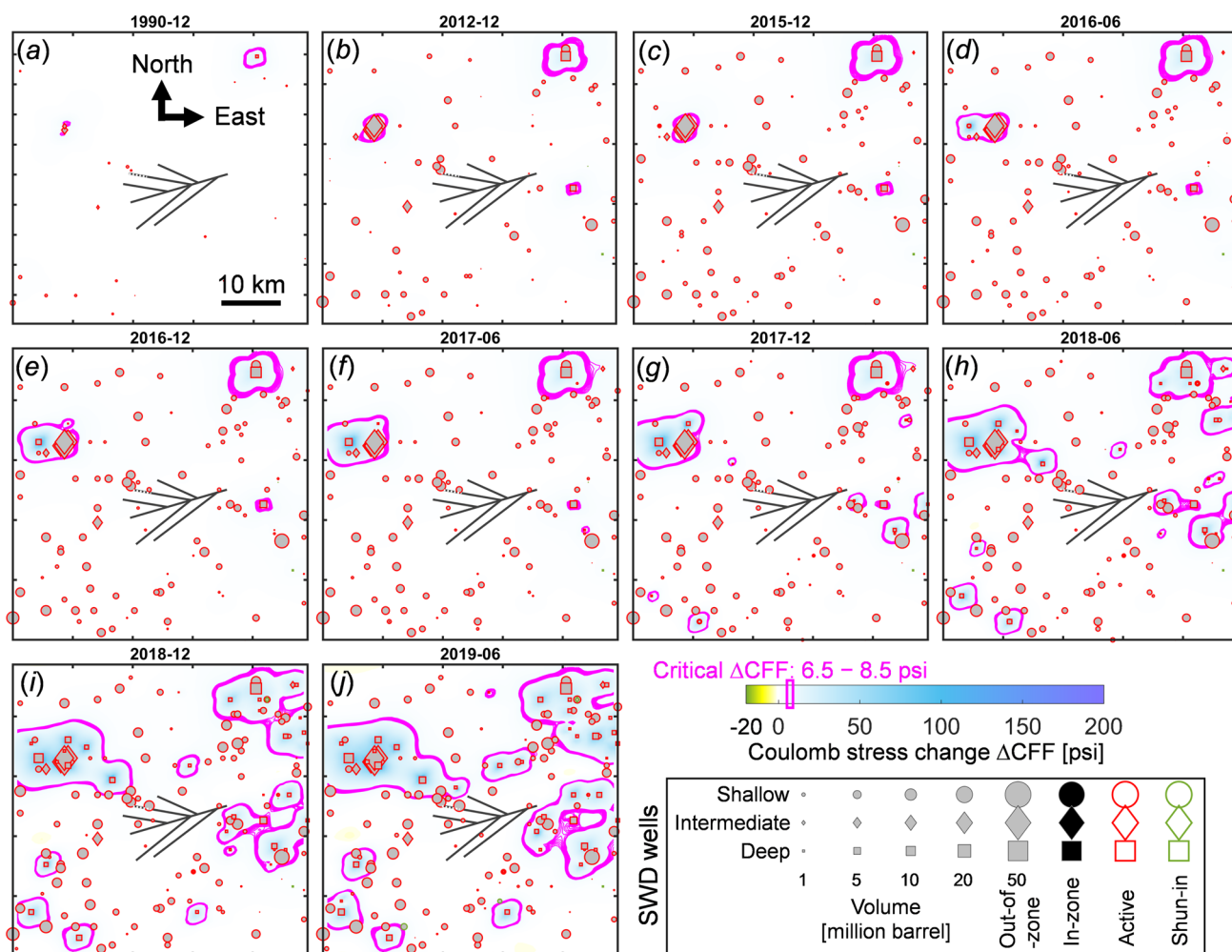


Fig. 14 Snapshots of modeled ΔCFF at the TOB taken at 10 chosen times **a–j** from December 1990 to June 2019. The iso-value contours are plotted from 6.5 to 8.5 psi at a 0.25 psi increment. All wells are

out-of-zone for this depth and shaded in grey accordingly. The results are generated using scenario 3a to illustrate historical stressing and are nearly identical for scenario 3b

patch A. In scenario 2a, patch A developed to the Northwest and extended into the basement. A small portion of seismicity resided within patch A but the majority laid ahead by a few kilometers, leading to an overall suboptimal matching in 3D. In scenario 2b and on the North side, patch A developed to a larger extent, including the main lobe similar to that in scenario 2a but expanded and a secondary lobe to the Southeast resulting from well #1. Here, the upper periphery of the seismicity cloud agrees with the distribution of critical areas; the Woo and Ellsworth (2023) catalog and the Nanometrics catalog, splitting toward the Northwest and the Southeast as they approach the TOB, coincide with the main lobe and the secondary lobe, respectively. In scenario 2b and on the South side, the result resembles that of scenario 2a with unsatisfactory matching. Overall, scenario 2b better explains the distribution of seismicity within the Coulomb faulting framework and is more plausible; it also suggests that seismicity nucleated on the North side of fault #2.

4.2.6 Nucleation Effect

The modeling outcomes in scenarios 2a and 2b so far have partially explained seismicity onset and distribution within the Coulomb faulting framework, but some aspects remain perplexing. Figure 9j, Fig. 10a–c, and Fig. 11a–c show that the arrival of the historical portion of the critical ΔCFF on fault #2 preceded the onset of seismicity by one to half year depending on the interpretation of the dashed segment. From June to December 2020, a segment just to the East of well #23 and another segment near the right end of the fault have been subjected to critical Coulomb stressing. The absence of seismicity over this period likely reflects a time-dependent nucleation effect driven by rate-and-state friction (Segall and Lu 2015). The duration of a nucleation phase can range from years to days or minutes (Snell et al. 2020), and a similar half-year lag has been modeled for a hydrocarbon-producing reservoir in Acosta et al. (2023). Considering the

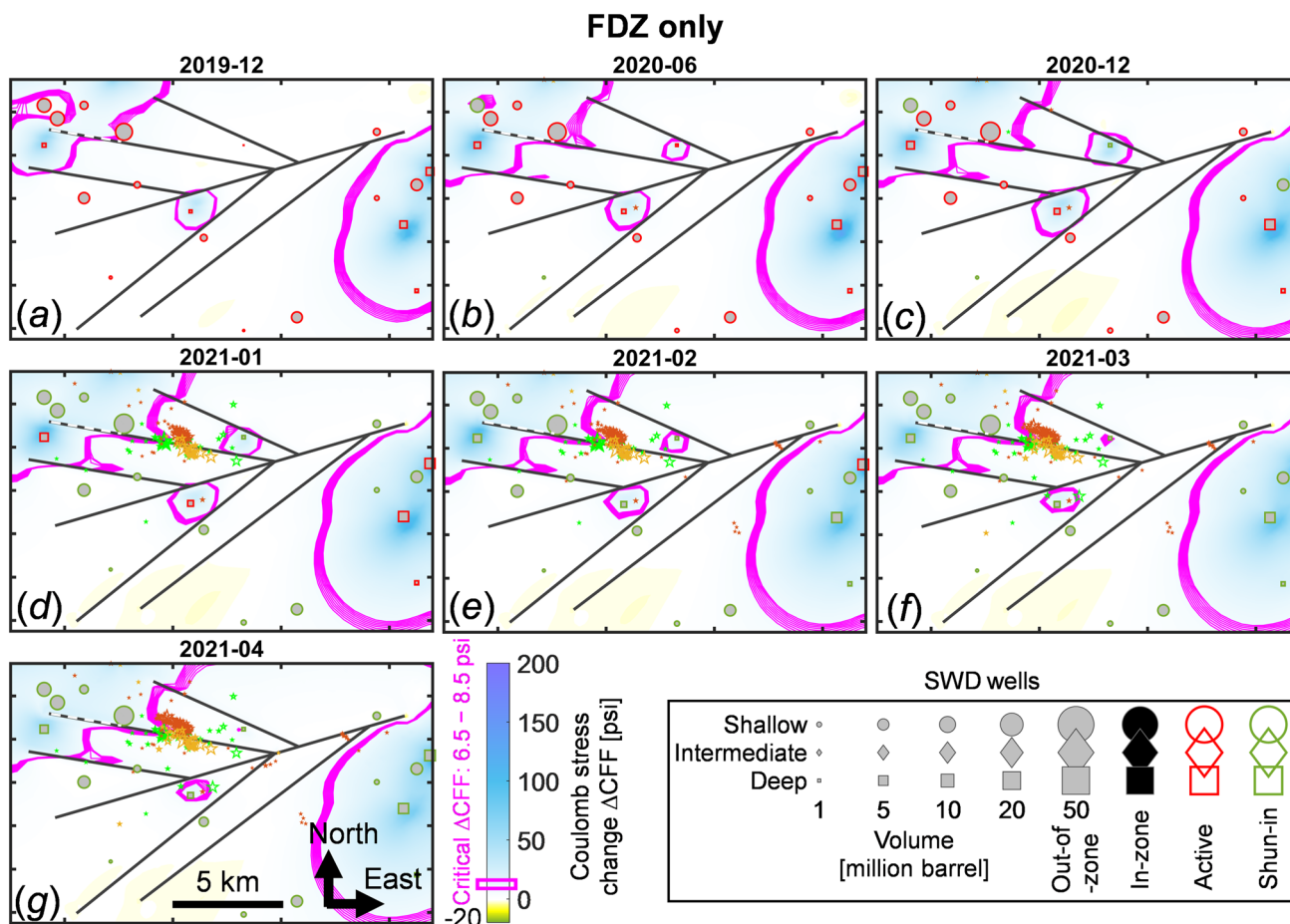


Fig. 15 Snapshots of modeled ΔCFF at the TOB and near the faults in scenario 3a taken at seven chosen recent times **a–g** from December 2019 to April 2021. The iso-value contours are plotted from 6.5 to 8.5

psi at a 0.25 psi increment. All wells are out-of-zone for this depth and shaded in grey accordingly. The results illustrate recent and near-fault stressing in scenario 3a (Color figure online)

nucleation effect might also better explain the events away from the upper periphery of the seismicity cluster that is not sufficiently explained by the Coulomb faulting analysis alone, see Fig. 12c, f, and i. To explore this, we cast the Coulomb stress changes on fault #2 into the rate-and-state friction framework and model relative seismicity rate R using a of 0.005 and 0.015, respectively, as the lower and upper bounds, following Sect. 3.3. For the case of $a = 0.005$, we display the distribution of R in Fig. 13a–i in the same way as in Fig. 12; for the case of $a = 0.015$, we only show the results at the seismicity onset time, see Fig. 13j–l. By January 2021 and irrespective of the a value, the fault was partitioned into three patches, labeled with I, II, and III, in scenario 2a and the North side in scenario 2b. Cross-referencing among Fig. 10a, b, d, Fig. 10a, b, d, Fig. 12, and Fig. 13a–i shows that patches I and III originated from the historical stressing arrived from the Northwest and the recent stressing by well #1, respectively; together, they drove the forming of the funnel-shaped patch II in between, which developed over a half-year period from June 2020 to January

2021. This agrees with the half-year lag mentioned above. Moreover, the shape of patch II in either scenario agrees well with the distribution of the remaining seismicity beyond the near-critical patch A. Together, these agreements reaffirm the plausibility of the two scenarios and evidence the nucleation effect.

Meanwhile, the two scenarios are different in their plausibility. In scenario 2a, the highest seismicity rate was always registered on patch I throughout time, see Fig. 13a–c, j, but most of the seismicity was outside this patch. While interpreting the uncertain segment as part of the rock provides a viable explanation, scenario 2b reconciles this mismatch. Here, at the seismicity onset time and on the North side of the fault, the highest seismicity rate was indeed registered on patch II, with an increase by nearly three orders of magnitude relative to the background rate in the case of a lower a value (Fig. 13f), whereas patch I tends to diminish with a higher a value (Fig. 13k); on the south side, the seismicity distribution was misaligned with the modeled seismicity rate. Thus, between the two scenarios, the results here again

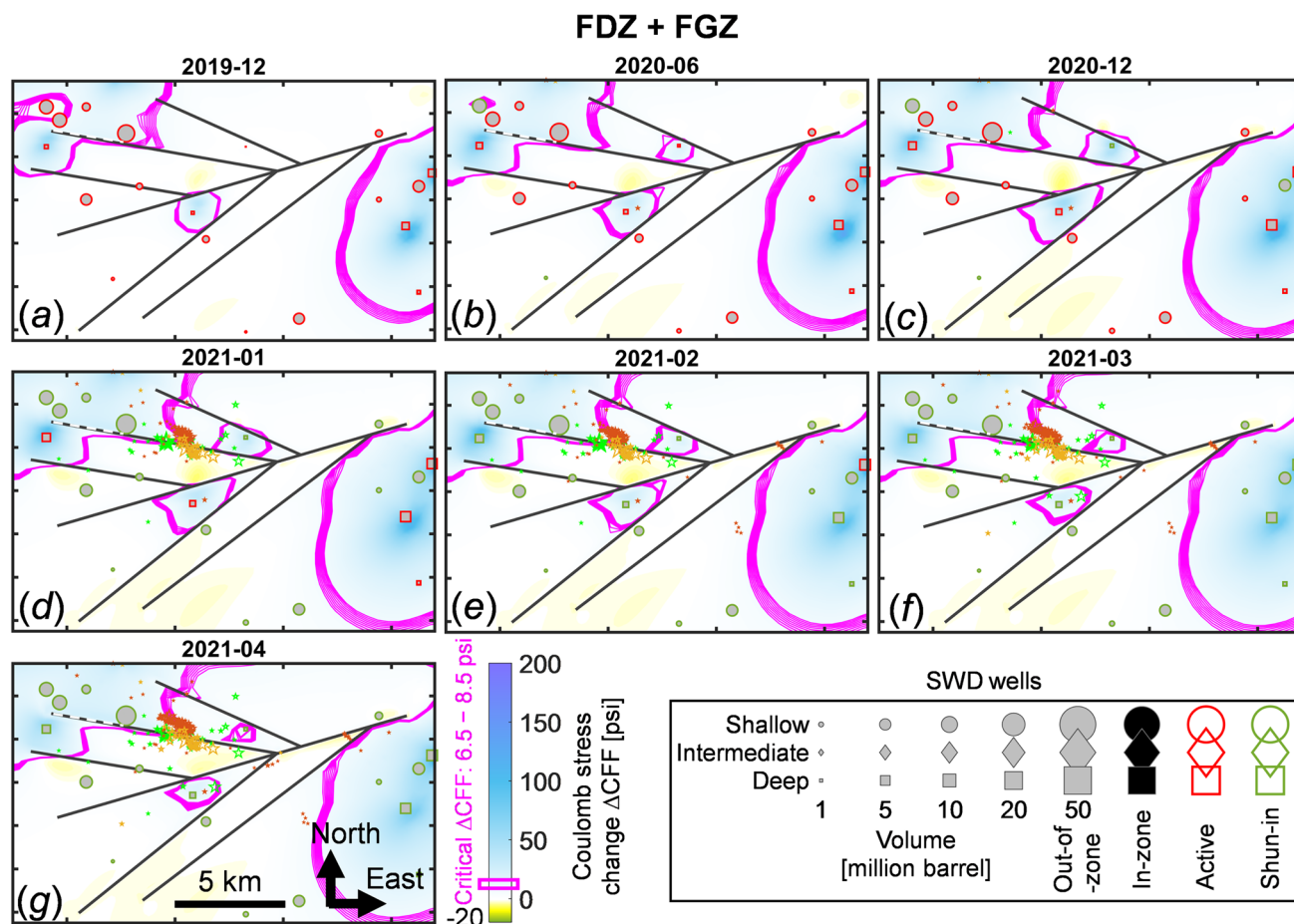


Fig. 16 Snapshots of modeled Δ CFF at the TOB and near the faults in scenario 3b taken at the same seven chosen recent times a–g from December 2019 to April 2021, highlighting the amplification effect on the critical Δ CFF when compared to scenario 3a

favor scenario 2b and suggest that seismicity nucleated on the North side of the fault. The a value tends to be near the lower end (~ 0.005), which agrees with the microphysically derived value of around 0.006 (Chen et al. 2017).

4.3 Scenarios 3a and 3b: Basement-Rooted Faults Terminating at the Top of Basement

We repeat the same analysis done in Sect. 4.2 here for scenarios 3a and 3b and test their plausibility. The critical depth is now the TOB itself where the highest CFF increases are met with the lowest triggering threshold on the seismogenic fault. Figure 14a–j show the evolution of CFF changes and the propagation of the critical Δ CFF at the TOB and chosen times from December 1990 to June 2019. These historical changes are common between scenarios 3a and 3b. At this depth, the CFF changes were below 50 psi, only a fraction of those in the DVEB, and the earthquake-triggering threshold is slightly higher at 7.7 psi, surrounding which we show the iso-value contours from 6.5 to 8.5 psi at a 0.25 psi

increment. Compared to scenarios 2a and 2b (see Fig. 9), we observe similarly little impact from the shallow injection on the historical stressing at the TOB; the difference is that only the first group of wells to the Northwest, containing all the intermediate wells and some deep wells as identified in Sect. 4.2.2, acted as contributing sources, whereas the second group of deep wells to the Northeast became irrelevant due to their critical Δ CFF not reaching the faults. This continued to be the case following the recent propagation of the critical Δ CFF toward and along fault #2 between December 2019 and April 2021, as depicted in Fig. 15a–g for scenario 3a and Fig. 16a–g for scenario 3b. Also seen over this period is that while the relevant critical Δ CFF portion arriving from the Northwest overall lagged in the hosting rock when compared to Figs. 10 and 11, it was nevertheless accelerated by the FDZs toward the seismogenic segment of fault #2, agreeing with the event distribution. Thus, the basement-to-DVEB hydraulic connection itself appears to be more important than the extent of the connection in triggering seismicity. In scenario 3b, we again observe the amplification effect

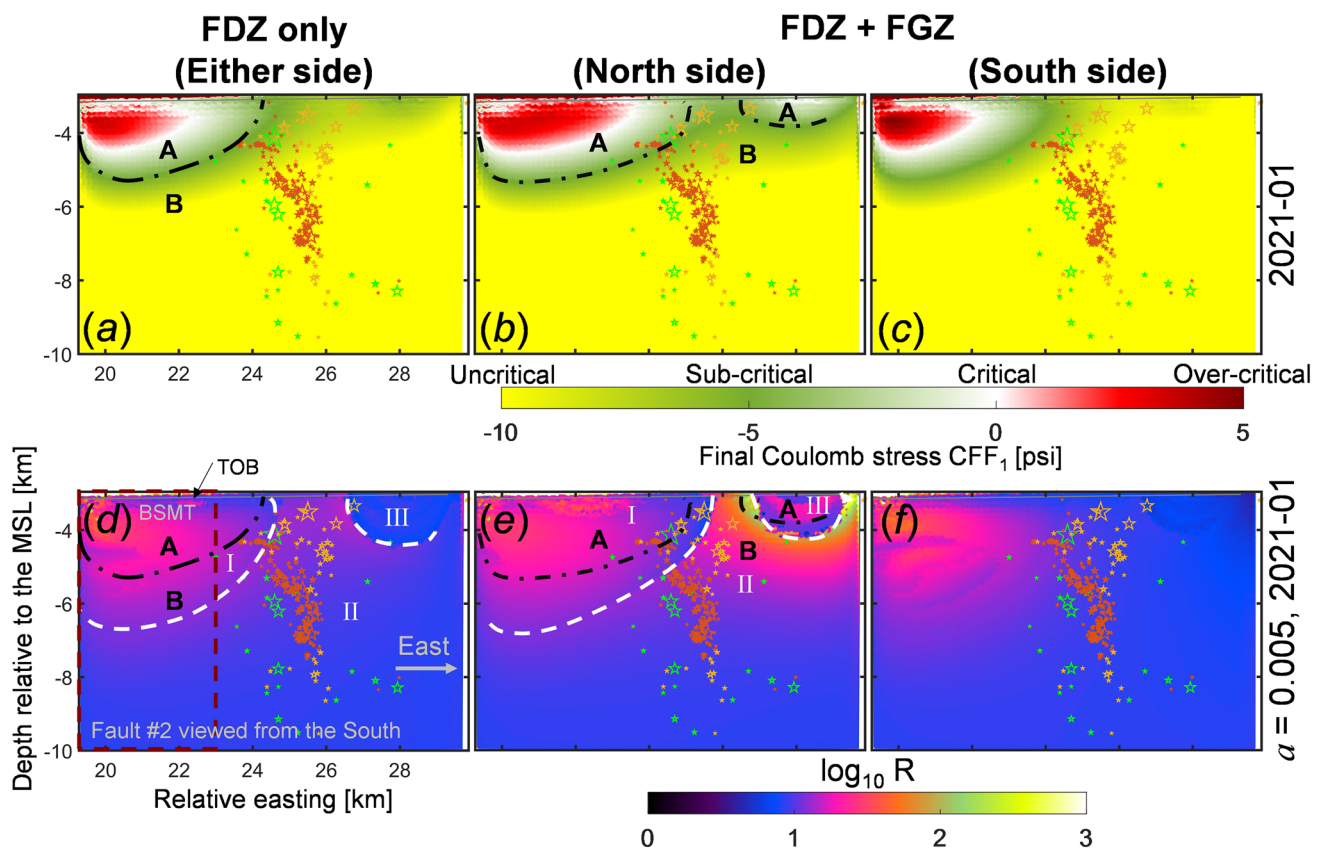


Fig. 17 North-facing snapshots of CFF_1 on fault #2 taken in January 2021, for scenario 3a **a** and scenario 3b North side **b** and South side **c**. The fault has only a basement segment. The colors and patches A and B have the same meaning as in Fig. 12. **d–f** The correspond-

ing relative seismicity rate modeled using an a value of 0.005, and patches I, II, and III are labeled in the same way as in Fig. 13. The uncertain segment of fault #2 is indicated with a dashed box in dark red (Color figure online)

on the critical ΔCFF due to the sealing fault-zone structure. In both scenarios 3a and 3b, the near-fault well #1 critically stressed fault #2 at the mainshock time whereas wells #2 did not due to containment by the non-seismogenic faults #4 and #5, similar to in scenarios 2a and 2b; in scenario 3b, the critical ΔCFF portion generated by well #1 did not quite coalesce with the main portion, unlike in scenario 2b. Overall, scenarios 3a and 3b and scenarios 2a and 2b resembled in terms of source disposal intervals and shared some contributing wells but differed in earthquake initiation depth, number of source stressors, stressing history, and seismicity triggering processes. Despite these differences, where the critical ΔCFF intersected fault #2 at the event origin time in scenarios 3a and 3b satisfactorily matched event epicentral locations. Thus, these two scenarios are also plausible.

Like before, we analyze the seismicity distribution in relation to the modeled final Coulomb stress and relative seismicity rate on fault #2 to further test and differentiate the plausibility of scenarios 3a and 3b and identify potential nucleation processes. The results at various times exhibit

similarities to those in Figs. 12 and 13, and are only displayed at the seismicity onset time in January 2021, see Fig. 17. Figure 17a–c are the counterparts of Fig. 12c, f, and i and show the distribution of CFF_1 on fault #2 for scenario 3a and the two sides of the fault in scenario 3b, with the near-critical patch A and the uncritical patch B marked. As can be seen, scenario 3b better explains the upper periphery and the bifurcation of seismicity near the TOB and, thus, is preferred over scenario 3a. In either scenario, the half- to 1-year lag in seismicity onset (see Figs. 15a–d and 16a–d) and the remaining seismicity away from the TOB are explained by the nucleation effect, see Fig. 17d–f, which are the counterparts of Fig. 13c, f, and i. Here, the a value is 0.005 as established in Sect. 4.2.6. The nucleation effect drives seismicity in a funnel zone captured by patch II. Scenario 3b again hindcasted the highest seismicity rate on patch II on the North side, which better agrees with the data than scenario 3a. This reaffirms the plausibility of scenario 3b and suggests that seismicity nucleated on the North side.

5 Conclusions

We draw the following key findings through this investigation.

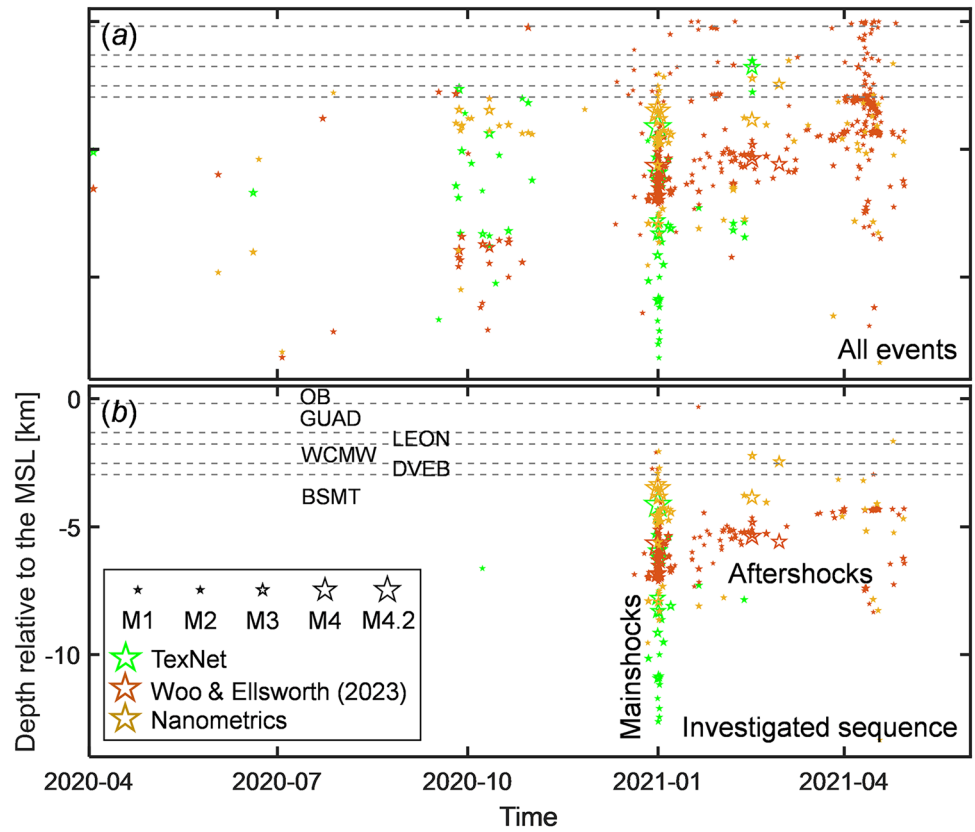
1. This work strongly suggests that the 2020 December Stanton, TX M 4.2 seismicity sequence was induced by SWD dating back over three decades in the central Midland Basin. The critical Coulomb stress changes at inferred seismogenic depths were driven mainly by deep and intermediate SWD and negligibly by shallow SWD.
2. The basement-rooted faults likely terminate at the top of the basement or extend into the overlying deep disposal interval but not the intermediate disposal interval nor the shallow disposal interval. The seismicity sequence was likely initiated by a Coulomb stress increase by 7–8 psi on a near-vertical seismogenic fault striking at $\sim N100^\circ E$.
3. Among the modeled 180+ SWD wells, only a small fraction (< 10%) acted as source stressors that contributed to the critical Coulomb stress increase at the inferred hypocentral locations and event origin time, including four historical intermediate wells to the Northwest, a few recent near-fault deep wells, and potentially several historical far-field deep wells to the Northeast, depending on the fault upper extent. Some other wells, although generated sufficiently high Coulomb stress increases capable of destabilizing the seismogenic fault, did not have ample time between the beginning of injection and the mainshock time to take effect. Other near-field wells, despite their proximity to seismicity, did not contribute, either, due to the diversion of pore pressure and poroelastic stresses by non-seismogenic faults.
4. In time, the Coulomb faulting analysis hindcasts the mainshock on the seismogenic section of the hosting fault but also suggests earlier seismicity on an adjacent fault segment, which was absent in the data. In space, the Coulomb faulting analysis explains the upper periphery of the seismicity cluster but not the remaining. These two discrepancies can be reasonably reconciled by considering the rate-and-state earthquake nucleation effect, which captures a potential half-year-long nucleation period and better explains the overall seismicity spatial distribution.
5. Either fault-zone structure is plausible, however, the modeling favors the scenarios with a fault comprising not only two permeable damage zones but also an impermeable gouge zone. The transversal sealing effect due to fault gouge amplifies along-fault pore pressure propagation and can lead to sudden coalescence of critical Coulomb stress, better agreeing with the spatial distribution of the epicenters and the evanescent nature of the main shock. Including the fault gouge also creates two instead of one critical Coulomb stress lobes on the seismogenic fault, agreeing better with the bifurcation of seismicity toward the top of the basement. The two lobes stemmed from a cluster of intermediate and deep wells to the Northwest and a deep well near the East fault tip, respectively. With the nucleation effect, the presence of fault gouge leads to a prominent seismicity funnel zone between the two Coulomb stress lobes, which better agrees with the seismicity spatial distribution. The earthquakes likely nucleated on the northern side of the seismogenic fault.
6. The shale formation tends to act as a seismicity barrier due to its differential stress relaxation, which decreases stress anisotropy and un-favors shear slip.

This work involves uncertainties in model parameters. Nevertheless, detailed data integration and analysis, combined with high-end numerical modeling and scenario testing, allow us to calibrate the model and make meaningful interpretations. Given the continuing seismicity in the Midland Basin, this work provides a paradigm for better understanding the causal links between SWD and seismicity and can inform the development of operator-led response plans aimed at mitigating seismicity.

A.1 Earthquakes in Time

See Fig. 18.

Fig. 18 Earthquake depth versus origin time. The events are sourced from three catalogs and sized by their magnitude. **a** All events in the area of study. **b** The seismicity sequence investigated in this study



A. 2 Initial CFF on Faults

See Table 1.

A. 3 Coulomb Stress Changes on Faults

See Fig. 19.

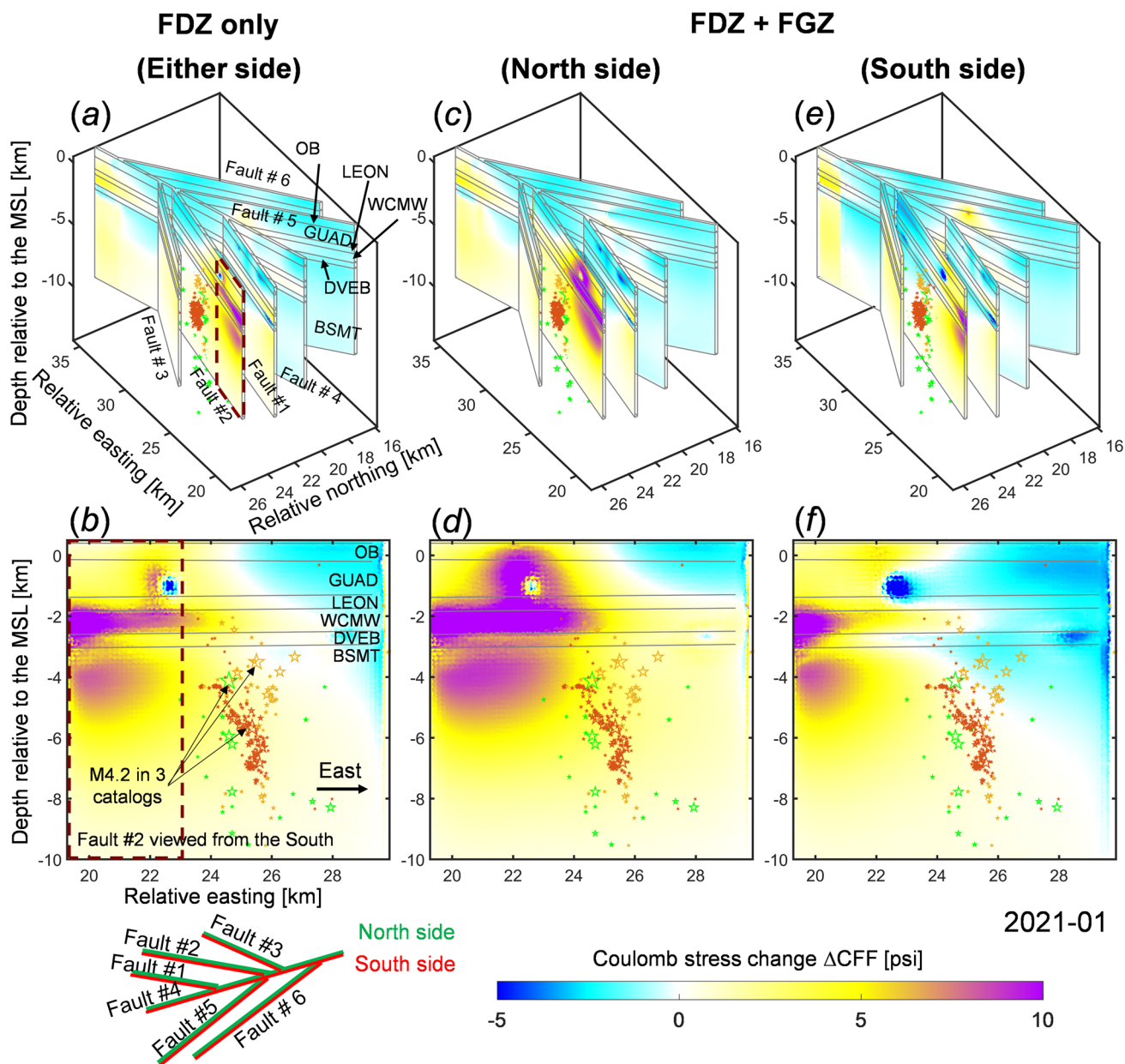


Fig. 19 Distribution of Coulomb stress changes on all faults in the 3D view (top row) and on the inferred seismogenic fault #2 in the North-facing side view (bottom row) for scenarios 1a **a–b** and 1b **c–f** at the mainshock time in January 2021. The intervals are indicated, and the

investigated earthquake sequence is overlaid. The uncertain segment of fault #2 is indicated with a dashed box. A map view of the faults is also given showing the North side in green and the South side in red (Color figure online)

Acknowledgements We thank the ExxonMobil management for permission to publish this work.

Author Contributions L. J. conceived the research, designed the methodology, wrote the code, analyzed the data, performed the modeling, analyzed the results, and wrote the paper. W. J. C. and S. A. H. collected and processed the data and reviewed the paper.

Funding This study received no external funding.

Data Availability The injection data can be downloaded in origin form from the Texas Railroad Commission website (<https://webapps.rrc.texas.gov/H10/h10PublicMain.do>) or in curated form from B3 Insight (<https://www.b3insight.com/>) with a subscription. The TexNet catalog is accessible at <https://www.beg.utexas.edu/texnet-cisr/texnet/earthquake-catalog>, the Woo and Ellsworth (2023) catalog is available at <https://doi.org/https://doi.org/10.1785/0120230086>, and the Nanometrics catalog can be obtained from <https://nanometrics.ca/home> with a subscription. The formation and fault data can be obtained from <https://www.beg.utexas.edu/texnet-cisr>. Other data are available from the corresponding author upon request.

Declarations

Conflict of interest The authors declare that they have no conflict of interest regarding the publication of this paper.

Open Access This article is licensed under a Creative Commons Attribution-NonCommercial-NoDerivatives 4.0 International License, which permits any non-commercial use, sharing, distribution and reproduction in any medium or format, as long as you give appropriate credit to the original author(s) and the source, provide a link to the Creative Commons licence, and indicate if you modified the licensed material. You do not have permission under this licence to share adapted material derived from this article or parts of it. The images or other third party material in this article are included in the article's Creative Commons licence, unless indicated otherwise in a credit line to the material. If material is not included in the article's Creative Commons licence and your intended use is not permitted by statutory regulation or exceeds the permitted use, you will need to obtain permission directly from the copyright holder. To view a copy of this licence, visit <http://creativecommons.org/licenses/by-nc-nd/4.0/>.

References

- Acosta M, Avouac JP, Smith JD, Sirorattanakul K, Kaveh H, Bourne SJ (2023) Earthquake nucleation characteristics revealed by seismicity response to seasonal stress variations induced by gas production at Groningen. *Geophys Res Lett* 50(19):e2023GL105455
- Altmann JB, Müller TM, Müller BI, Tingay MR, Heidbach O (2010) Poroelastic contribution to the reservoir stress path. *Int J Rock Mech Min Sci* 47(7):1104–1113
- Barbour AJ, Norbeck JH, Rubinstein JL (2017) The effects of varying injection rates in Osage County, Oklahoma, on the 2016 M w 5.8 Pawnee earthquake. *Seismol Res Lett* 88(4):1040–1053
- Biot MA (1941) General theory of three-dimensional consolidation. *J Appl Phys* 12(2):155–164
- Bolton DC, Affinito R, Smye K, Marone C, Hennings P (2023) Frictional and poromechanical properties of the Delaware mountain group: insights into induced seismicity in the Delaware Basin. *Earth Planet Sci Lett* 623:118436
- Borja RI (2006) On the mechanical energy and effective stress in saturated and unsaturated porous continua. *Int J Solids Struct* 43(6):1764–1786
- Byerlee J (1978) Friction of rocks. *Rock Frict Earthq Pred* 1978:615–626
- Chang KW, Segall P (2016) Injection-induced seismicity on basement faults including poroelastic stressing. *J Geophys Res Solid Earth* 121(4):2708–2726
- Chang KW, Yoon H (2020) Hydromechanical controls on the spatiotemporal patterns of injection-induced seismicity in different fault architecture: implication for 2013–2014 Azle earthquakes. *J Geophys Res Solid Earth* 125(9):e2020JB020402
- Chang KW, Yoon H (2022) Permeability-controlled migration of induced seismicity to deeper depths near Venus in North Texas. *Sci Rep* 12(1):1382
- Chen J, Niemeijer AR, Spiers CJ (2017) Microphysically derived expressions for rate-and-state friction parameters, a, b, and Dc. *J Geophys Res Solid Earth* 122(12):9627–9657
- Chen X, Haffener J, Goebel TH, Meng X, Peng Z, Chang JC (2018) Temporal correlation between seismic moment and injection volume for an induced earthquake sequence in central Oklahoma. *J Geophys Res Solid Earth* 123(4):3047–3064
- Chen R, Xue X, Park J, Datta-Gupta A, King MJ (2020) New insights into the mechanisms of seismicity in the Azle area North Texas. *Geophysics* 85(1):EN1–EN15
- COMSOL (2014) COMSOL Multiphysics User's Guide, COMSOL AB, Burlington, Mass
- Coussy O (2004) Poromechanics. Wiley, New York
- Dahm T, Hainzl S (2022) A Coulomb stress response model for time-dependent earthquake forecasts. *J Geophys Res Solid Earth* 127(9):e2022JB024443
- Davis SD, Frohlich C (1993) Did (or will) fluid injection cause earthquakes?-criteria for a rational assessment. *Seismol Res Lett* 64(3–4):207–224
- Dempsey D, Suckale J (2017) Physics-based forecasting of induced seismicity at Groningen gas field, the Netherlands. *Geophys Res Lett* 44(15):7773–7782
- Deng K, Liu Y, Harrington RM (2016) Poroelastic stress triggering of the december 2013 Crooked Lake, Alberta, induced seismicity sequence. *Geophys Res Lett* 43(16):8482–8491
- Dieterich J (1994) A constitutive law for rate of earthquake production and its application to earthquake clustering. *J Geophys Res Solid Earth* 99(B2):2601–2618
- DSS (Dassault Systèmes Simulia) (2014) Abaqus Theory Manual Version 6.11
- Ellsworth WL (2013) Injection-induced earthquakes. *Science* 341(6142):1225942
- Fan Z, Eichhubl P, Gale JF (2016) Geomechanical analysis of fluid injection and seismic fault slip for the Mw4. 8 Timpson, Texas, earthquake sequence. *J Geophys Res Solid Earth* 121(4):2798–2812
- Fang X, Chen T, Li S, Brooks N, Knapo G, Huffman AR, Stornio R (2024) Evaluating the effects of velocity models and array configuration on induced seismic event locations in the Permian Basin. *Geophysics* 89(1):L1–L20
- Frohlich C, Hayward C, Stump B, Potter E (2011) The dallas-fort worth earthquake sequence: october 2008 through May 2009. *Bull Seismol Soc Am* 101(1):327–340
- Frohlich C, DeShon H, Stump B, Hayward C, Hornbach M, Walter JI (2016) A historical review of induced earthquakes in Texas. *Seismol Res Lett* 87(4):1022–1038
- Ge S, Saar MO (2022) Induced seismicity during geoeenergy development—a hydromechanical perspective. *J Geophys Res Solid Earth* 127(3):e2021JB023141
- Goebel THW, Weingarten M, Chen X, Haffener J, Brodsky EE (2017) The 2016 Mw5. 1 Fairview, Oklahoma earthquakes: evidence for long-range poroelastic triggering at > 40 km from fluid disposal wells. *Earth Planet Sci Lett* 472:50–61
- Grigoli F, Cesca S, Rinaldi AP, Manconi A, Lopez-Comino JA, Clinton JF, Wiemer S (2018) The november 2017 M w 5.5 Pohang earthquake: a possible case of induced seismicity in South Korea. *Science* 360(6392):1003–1006
- Grigoratos I, Rathje E, Bazzurro P, Savvaidis A (2020) Earthquakes induced by wastewater injection, part II: statistical evaluation of causal factors and seismicity rate forecasting. *Bull Seismol Soc Am* 110(5):2483–2497
- Haddad M, Eichhubl P (2020) Poroelastic models for fault reactivation in response to concurrent injection and production in stacked reservoirs. *Geomech Energy Environ* 24:100181
- Haddad M, Eichhubl P (2023) Fault reactivation in response to saltwater disposal and hydrocarbon production for the Venus, TX, M w 4.0 Earthquake sequence. *Rock Mech Rock Eng* 56(3):2103–2135
- Harris RA, Simpson RW (1992) Changes in static stress on southern California faults after the 1992 Landers earthquake. *Nature* 360(6401):251–254

- Heimisson ER, Smith JD, Avouac JP, Bourne SJ (2022) Coulomb threshold rate-and-state model for fault reactivation: application to induced seismicity at Groningen. *Geophys J Int* 228(3):2061–2072
- Hill RG, Weingarten M, Rockwell TK, Fialko Y (2023) Major southern san andreas earthquakes modulated by lake-filling events. *Nature* 618(7966):761–766
- Hill RG, Weingarten M, Langenbruch C, Fialko Y (2024) Mitigation and optimization of induced seismicity using physics-based forecasting. arXiv preprint [arXiv:2403.10675](https://arxiv.org/abs/2403.10675)
- Horne EA, Hennings PH, Smye KM, Calle AZ, Morris AP, Huang GCD (2024) Interpretation, characterization and slip hazard assessment of faults in the Midland Basin, West Texas, United States. *AAPG Bulletin*, (20,240,201)
- Hsieh PA, Bredehoeft JD (1981) A reservoir analysis of the Denver earthquakes: a case of induced seismicity. *J Geophys Res Solid Earth* 86(B2):903–920
- Hughes TJ (2012) *The finite element method: linear static and dynamic finite element analysis*. Courier Corporation
- Hui G, Chen S, Chen Z, He Y, Wang S, Gu F (2021) Investigation on two Mw 3.6 and Mw 4.1 earthquakes triggered by poroelastic effects of hydraulic fracturing operations near crooked lake, Alberta. *J Geophys Res Solid Earth* 126(5):e2020JB020308
- Hurd O, Zoback MD (2012) Intraplate earthquakes, regional stress and fault mechanics in the central and eastern US and Southeastern Canada. *Tectonophysics* 581:182–192
- Improta L, Valoroso L, Piccinini D, Chiarabba C (2015) A detailed analysis of wastewater-induced seismicity in the Val d’Agri oil field (Italy). *Geophys Res Lett* 42(8):2682–2690
- Jaeger JC, Cook NGW (1979) *Fundamentals of rock mechanics*. Chapman and Hall, London
- Jin L (2022) A hydromechanical-stochastic approach to modeling fluid-induced seismicity in arbitrarily fractured poroelastic media: effects of fractures and coupling. *Tectonophysics* 826:229249
- Jin L, Zoback MD (2017) Fully coupled nonlinear fluid flow and poroelasticity in arbitrarily fractured porous media: a hybrid-dimensional computational model. *J Geophys Res Solid Earth* 122(10):7626–7658
- Jin L, Zoback MD (2018) Fully dynamic spontaneous rupture due to quasi-static pore pressure and poroelastic effects: an implicit nonlinear computational model of fluid-induced seismic events. *J Geophys Res Solid Earth* 123(11):9430–9468
- Jin L (2023) On a saturated poromechanical framework and its relation to abaqus soil mechanics and biot poroelasticity frameworks. arXiv preprint [arXiv:2304.02148](https://arxiv.org/abs/2304.02148)
- Jin L, Curry WJ, Lippoldt RC, Hussenoeder SA, Bhargava P (2023) 3D coupled hydro-mechanical modeling of multi-decadal multi-zone saltwater disposal in layered and faulted poroelastic rocks and implications for seismicity: an example from the Midland Basin. *Tectonophysics* 863:229996
- Juanes R, Jha B, Hager BH, Shaw JH, Plesch A, Astiz L, Frohlich C (2016) Were the may 2012 emilia-romagna earthquakes induced? a coupled flow-geomechanics modeling assessment. *Geophys Res Lett* 43(13):6891–6897
- Keranen KM, Savage HM, Abers GA, Cochran ES (2013) Potentially induced earthquakes in Oklahoma, USA: links between wastewater injection and the 2011 Mw 5.7 earthquake sequence. *Geology* 41(6):699–702
- Keranen KM, Weingarten M, Abers GA, Bekins BA, Ge S (2014) Sharp increase in central Oklahoma seismicity since 2008 induced by massive wastewater injection. *Science* 345(6195):448–451
- Kim WY (2013) Induced seismicity associated with fluid injection into a deep well in Youngstown, Ohio. *J Geophys Res Solid Earth* 118(7):3506–3518
- Kohli A, Zoback M (2021) Stratigraphically controlled stress variations at the hydraulic fracture test site-1 in the midland basin. *TX Energies* 14(24):8328
- Langenbruch C, Zoback MD (2016) How will induced seismicity in Oklahoma respond to decreased saltwater injection rates? *Sci Adv* 2(11):e1601542
- Langenbruch C, Weingarten M, Zoback MD (2018) Physics-based forecasting of man-made earthquake hazards in Oklahoma and Kansas. *Nat Commun* 9(1):3946
- Lund Sneek JE, Zoback MD (2018) State of stress in the Permian Basin, Texas and New Mexico: implications for induced seismicity. *Lead Edge* 37(2):127–134
- Ma X, Zoback MD (2020) Predicting lithology-controlled stress variations in the Woodford shale from well log data via viscoplastic relaxation. *SPE J* 25(05):2534–2546
- Murad MA, Loula AF (1994) On stability and convergence of finite element approximations of Biot’s consolidation problem. *Int J Numer Meth Eng* 37(4):645–667
- National Research Council. (2013) *Induced seismicity potential in energy technologies*. National Academies Press
- Norbeck JH, Rubinstein JL (2018) Hydromechanical earthquake nucleation model forecasts onset, peak, and falling rates of induced seismicity in Oklahoma and Kansas. *Geophys Res Lett* 45(7):2963–2975
- Ortiz JP, Person MA, Mozley PS, Evans JP, Bilek SL (2019) The role of fault-zone architectural elements on pore pressure propagation and induced seismicity. *Groundwater* 57(3):465–478
- Peterie SL, Miller RD, Intfen JW, Gonzales JB (2018) Earthquakes in Kansas induced by extremely far-field pressure diffusion. *Geophys Res Lett* 45(3):1395–1401
- Railroad Commission of Texas Oil and Gas Division (2022) *Seismicity Response*. <https://www.rrc.texas.gov/oil-and-gas/applications-and-permits/injection-storage-permits/oil-and-gas-waste-disposal/injection-disposal-permit-procedures/seismicity-review/seismicity-response/>
- Rice JR, Cleary MP (1976) Some basic stress diffusion solutions for fluid-saturated elastic porous media with compressible constituents. *Rev Geophys* 14(2):227–241
- Rozhko AY (2010) Role of seepage forces on seismicity triggering. *J Geophys Res Solid Earth* 115(B11):1
- Rubinstein JL, Ellsworth WL, McGarr A, Benz HM (2014) The 2001–present induced earthquake sequence in the Raton Basin of northern New Mexico and southern Colorado. *Bull Seismol Soc Am* 104(5):2162–2181
- Rudnicki JW (1986) Fluid mass sources and point forces in linear elastic diffusive solids. *Mech Mater* 5(4):383–393
- Savvaiddis A, Young B, Huang GCD, Lomax A (2019) TexNet: a statewide seismological network in Texas. *Seismol Res Lett* 90(4):1702–1715
- Savvaiddis A, Lomax A, Breton C (2020) Induced seismicity in the Delaware Basin, West Texas, is caused by hydraulic fracturing and wastewater disposal. *Bull Seismol Soc Am* 110(5):2225–2241
- Schoenball M, Walsh FR, Weingarten M, Ellsworth WL (2018) How faults wake up: the Guthrie-Langston. *Okla Earthq Lead Edge* 37(2):100–106
- Segall P (2010) *Earthquake and volcano deformation*. Princeton University Press, Princeton
- Segall P, Lu S (2015) Injection-induced seismicity: poroelastic and earthquake nucleation effects. *J Geophys Res Solid Earth* 120(7):5082–5103
- Shapiro SA, Dinske C, Langenbruch C, Wenzel F (2010) Seismogenic index and magnitude probability of earthquakes induced during reservoir fluid stimulations. *Lead Edge* 29(3):304–309
- Sheng Y, Pepin KS, Ellsworth WL (2022) On the depth of Earthquakes in the delaware basin: a case study along the reeves-pecos county line. *Seism Rec* 2(1):29–37
- Shirzaei M, Manga M, Zhai G (2019) Hydraulic properties of injection formations constrained by surface deformation. *Earth Planet Sci Lett* 515:125–134

- Skoumal RJ, Trugman DT (2021) The proliferation of induced seismicity in the Permian Basin, Texas. *J Geophys Res Solid Earth* 126(6):e2021JB021921
- Skoumal RJ, Kaven JO, Barbour AJ, Wicks C, Brudzinski MR, Cochran ES, Rubinstein JL (2021) The induced Mw 5.0 March 2020 west Texas seismic sequence. *J Geophys Res Solid Earth* 126(1):e2020JB020693
- Smith JD, Avouac JP, White RS, Copley A, Gualandi A, Bourne S (2019) Reconciling the long-term relationship between reservoir pore pressure depletion and compaction in the Groningen region. *J Geophys Res Solid Earth* 124(6):6165–6178
- Smith JD, Heimisson ER, Bourne SJ, Avouac JP (2022) Stress-based forecasting of induced seismicity with instantaneous earthquake failure functions: applications to the Groningen gas reservoir. *Earth Planet Sci Lett* 594:117697
- Smye KM, Hennings PH, Horne EA (2021) Variations in vertical stress in the Permian Basin region. *AAPG Bull* 105(10):1893–1907
- Snell T, De Paola N, van Hunen J, Nielsen S, Collettini C (2020) Modelling fluid flow in complex natural fault zones: implications for natural and human-induced earthquake nucleation. *Earth Planet Sci Lett* 530:115869
- Sone H, Zoback MD (2014) Time-dependent deformation of shale gas reservoir rocks and its long-term effect on the in situ state of stress. *Int J Rock Mech Min Sci* 69:120–132
- Szafrański D, Duan B (2020) Exploring physical links between fluid injection and nearby earthquakes: the 2012 Mw 4.8 timpson, Texas, case study. *Bull Seismol Soc Am* 110(5):2350–2365
- Tan X, Lui SK (2023) Potential poroelastic triggering of the 2020 M 5.0 mentone earthquake in the delaware basin, Texas, by shallow injection wells. *Bull Seismol Soc Am*. <https://doi.org/10.1785/0120230142>
- TexNet (2021) Earthquake Catalog. <https://www.beg.utexas.edu/texnet-cisr/texnet/earthquake-catalog>
- Townend J, Zoback MD (2000) How faulting keeps the crust strong. *Geology* 28(5):399–402
- Tung S, Zhai G, Shirzaei M (2021) Potential link between 2020 Mentone, West Texas M5 earthquake and nearby wastewater injection: implications for aquifer mechanical properties. *Geophys Res Lett* 48(3):e2020GL090551
- Walsh FR III, Zoback MD (2015) Oklahoma's recent earthquakes and saltwater disposal. *Sci Adv* 1(5):e1500195
- Wang HF (2000) Theory of linear poroelasticity with applications to geomechanics and hydrogeology, vol 2. Princeton University Press, Princeton
- Wang TA, Dunham EM (2022) Hindcasting injection-induced aseismic slip and microseismicity at the cooper basin enhanced geothermal systems project. *Sci Rep* 12(1):19481
- Wang R, Kumpel HJ (2003) Poroelasticity: efficient modeling of strongly coupled, slow deformation processes in a multilayered half-space. *Geophysics* 68(2):705–717
- Wang B, Verdecchia A, Kao H, Harrington RM, Liu Y, Yu H (2021) A study on the largest hydraulic fracturing induced earthquake in Canada: numerical modeling and triggering mechanism. *Bull Seismol Soc Am* 111(3):1392–1404
- Wesson RL, Nicholson C (1987) Earthquake hazard associated with deep well injection; a report to the US Environmental Protection Agency (No. 87–331). US Geological Survey
- White JA, Borja RI (2008) Stabilized low-order finite elements for coupled solid-deformation/fluid-diffusion and their application to fault zone transients. *Comput Methods Appl Mech Eng* 197(49–50):4353–4366
- Woo JU, Ellsworth WL (2023) Reactivation of precambrian faults by deep wastewater injection in midland basin, texas, and performance evaluation of seismic response areas. *Bull Seismol Soc Am* 113(6):2543–2556
- Xu S, Rassouli F, Zoback M (2017) Utilizing a viscoplastic stress relaxation model to study vertical hydraulic fracture propagation in Permian Basin. In: SPE/AAPG/SEG unconventional resources technology conference. OnePetro
- Xu S, Singh A, Zoback MD (2019) Variation of the least principal stress with depth and its effect on vertical hydraulic fracture propagation during multi-stage hydraulic fracturing. In: 53rd US Rock Mechanics/Geomechanics Symposium. OnePetro
- Zhai G, Shirzaei M, Manga M (2021) Widespread deep seismicity in the Delaware Basin, Texas, is mainly driven by shallow wastewater injection. *Proc Natl Acad Sci* 118(20):e2102338118
- Zoback MD (2010) Reservoir geomechanics. Cambridge University Press, Cambridge

Publisher's Note Springer Nature remains neutral with regard to jurisdictional claims in published maps and institutional affiliations.